

CHARMED MESON PRODUCTION
IN 800 GeV P-P INTERACTIONS

Dissertation
by

Mark F. Senko



Department of Physics and Astronomy

VANDERBILT UNIVERSITY

Nashville, Tennessee 37235

CHARMED MESON PRODUCTION IN 800 GeV P-P INTERACTIONS

By

Mark Frederick Senko

Dissertation

Submitted to the Faculty of the
Graduate School of Vanderbilt University
in partial fulfillment of the requirements
for the degree of

DOCTOR OF PHILOSOPHY

in

Physics

May, 1989

Nashville, Tennessee

Approved:

Charles E. Rose
Thomas J. Weiler
R. F. Chenstorf
C. J. Maguire
Melvin J. Webster

Date:

Feb. 20, 1989
" " "
" " "
Feb 20, 1989
Feb 20, 1989

ACKNOWLEDGMENTS

After twenty-two years of school, the number of people to whom I owe gratitude is very large. I will refrain from listing all of my teachers starting at first grade, but I remember most of them, and thank them all. Special thanks are due to Mr. Leonard, my eighth grade physical science teacher at Bay Middle School, Bay Village, Ohio, whose enthusiasm started me on the road to a physics career. From Arkansas State University, Jonesboro, Arkansas, I give special thanks to Dr. Linnstaedter, whose faith was invaluable, and Dr. Mink, whose dedication and talent for teaching was inspirational. From Vanderbilt University, I thank Dr. Roos, my advisor, and Dr. Webster, my advisor-in-spirit. Also from Vanderbilt, I thank Dr. Marraffino and Dr. Waters for their humor, guidance, and friendship.

Many friendships were made with the graduate students who shared the experience of working on E743, and I would like to express thanks to each one: Andreas Roth, Gay Canough, Grace Mendez, Xi Liu, Ai Nguyen, Bertolt Vonck, and Christos Zabounidis. Special mention goes to Tom Dershem, who laughed at my jokes, and Mike Weber, who didn't. Mike and I were involved in more than our share of humorous incidents, though.

I would like to thank all of my friends at Vanderbilt, who made the day to day work of graduate school bearable. I would like to thank my wife, Mojgan, for her patience and love.

Above all, I would like to thank my parents for their lifelong support and encouragement.

TABLE OF CONTENTS

	Page
ACKNOWLEDGMENTS	ii
LIST OF FIGURES	vi
LIST OF TABLES	viii
 Chapter	
I. INTRODUCTION	1
Purpose	1
History	1
The Standard Model	2
Quantum Electrodynamics	3
Quantum Chromodynamics	6
Weak Theory	7
Electroweak Theory	8
Future Goals	9
II. THE PHYSICS OF CHARM.....	11
Prediction of Charm	11
Observation of Charm	13
Total Charm Hadroproduction Cross Sections	14
Differential Charm Hadroproduction Cross Sections	21
QCD Hadroproduction Models	23
The Fusion Model	23
The Flavor Excitation Model	25
The Intrinsic Charm Model	27
Charm Decays	28
The D^* Mesons	28
III. EXPERIMENTAL APPARATUS AND DATA AQUISITION.....	33
Introduction	33
The Beamline	33
The Bubble Chamber	34
The Spectrometer	35

The Magnet	35
Tracking Chambers	37
Particle Identification	37
The Trigger	41
IV. DATA ANALYSIS	43
Introduction	43
Scanning LEBC Film	43
Measuring LEBC Film	45
ADAM & EVA Measuring Machine	46
ERASME Measuring Machine	47
Synchronization	48
Track Reconstruction	49
Event Reconstruction	50
Track Hybridization	51
Track Recovery	52
Kinematics	60
Constraint Classes	64
Particle Identification	65
Čerenkov Radiation Detectors	66
Transition Radiation Detector	66
V. CHARM HADROPRODUCTION RESULTS	69
Total D/\bar{D} Cross Sections	69
Visibility Cuts and Weights	70
Results	72
Differential D/\bar{D} Cross Sections	73
Selection Criteria and Weights	73
Results	75
D^*/\bar{D}^* Meson Production	75
Analysis	78
Results	79
VI. CONCLUSIONS	83
D/\bar{D} Total Cross Section	83
D/\bar{D} Differential Cross Sections	84
D^*/\bar{D}^* Summary	86
APPENDIX	90
REFERENCES	92

LIST OF FIGURES

Figure	Page
1. Feynman diagrams for EM interactions	5
2. Feynman diagrams for QCD interactions	7
3. Feynman diagrams for weak interactions	8
4. Feynman diagrams for quark-antiquark annihilation and gluon fusion	24
5. Feynman diagrams for flavor excitation	26
6. Quark flow diagrams showing spectator decays of the charm quark.	29
7. Quark flow diagrams showing non-spectator decays of the charm quark	30
8. The E743 spectrometer configuration	36
9. The E743 trigger configuration	42
10. Mean error in $1/p$ for tracks with hits in the PX chamber	53
11. Mean error in $1/p$ for tracks without hits in the PX chamber	54
12. Example displays from E743PIX	57
13. Momenta of tracks found by FLOWERS	61
14. Momenta of tracks found by graphical techniques	62
15. Momenta of tracks found by RECOVERY	63
16. TRD reference distribution used in particle identification	68
17. The $d\sigma/dx_F$ distribution for D/\bar{D} mesons	76
18. The $d\sigma/dp_{\perp}^2$ distribution for D/\bar{D} mesons	77

19. Invariant mass plot showing the D^* mass peak and the superimposed background curve	81
20. Weighted invariant mass plot showing the D^* mass peak and the superimposed background curve	82
21. Energy dependence of the inclusive D/\bar{D} total cross section, normalized to $\sigma(D/\bar{D})$ at $\sqrt{s}=27.4$ GeV	85
22. Comparisons of the Fusion Model predictions to the measured $d\sigma/dx_F$ distribution	87
23. Comparisons of the Fusion Model predictions to the measured $d\sigma/dp_{\perp}^2$ distribution	88

LIST OF TABLES

Table	Page
1. Elementary Fermions.....	4
2. Elementary Gauge Bosons.....	4
3. Charmed $J^P = 0^-$ Mesons	15
4. Charmed $J^P = 1^-$ Mesons	15
5. Charmed $J^P = \frac{1}{2}^+$ Baryons	16
6. Charmed $J^P = \frac{3}{2}^+$ Baryons	17
7. Total Charm Particle Pair Production Cross Sections in Proton-Nucleon Interactions.....	19
8. Previous Results of the P_\perp and X_F dependence in D/\bar{D} Hadroproduction.....	22
9. D^* Decay Properties	31
10. Production of D and D^* Mesons	32
11. E743 Tracking Chamber Parameters.....	38
12. D/\bar{D} Cross Section Data Sample	72
13. D^* Data Sample	80
14. Energy Dependence of $\sigma(D/\bar{D})$	83

CHAPTER I

INTRODUCTION

Purpose

The purpose of this thesis is to present the results of a study of charmed-hadron production in proton-proton interactions at 800 GeV, and to interpret these results as a test of current theories of particle production. Data obtained at energies of $\sqrt{s} \leq 27.4$ GeV and $\sqrt{s} \geq 53$ GeV indicate a rapid rise in production cross sections, which is inconsistent with the current understanding of Quantum Chromodynamics. Our experiment, using the combined resources of CERN and Fermilab, provided data at the intermediate energy of $\sqrt{s} = 38.8$ GeV in an attempt to resolve the problem of the energy dependence of charmed-hadron production.

History

High Energy Physics is the study of elementary particles and their interactions. An elementary particle is a fundamental building block of matter, and as recently as fifty years ago only a few particles were thought to be elementary. These particles were the proton and neutron, which form the nucleus of an atom, the electron, which orbits the nucleus, the photon, and the neutrino, which appeared in some nuclear decays. As experiments at higher energies were performed in

an attempt to understand the force which binds the nucleus together, many new particles were discovered. It was eventually determined that these new particles, as well as the proton and neutron, were not elementary, but could be formed from different combinations of just three smaller particles, called quarks. Higher experimental energies provided data which suggested three more quarks, raising the total to six. The idea of quarks led to the development of what is now called the Standard Model.

The Standard Model

In the Standard Model, matter is composed of two types of fermions, particles with spin one-half, the quarks and the leptons. There are three leptons which have mass and a charge of $-|e|$, the electron, muon and tauon, each with a massless (or nearly massless) neutrino associated with it. There are three flavors of quarks with fractional charge $+2/3|e|$, the u , c , and t , and three flavors with fractional charge $-1/3|e|$, the d , s , and b . These quarks are commonly referred to as up, down, strange, charm, top and bottom. Each elementary fermion also has an antiparticle associated with it, which has the opposite charge of its partner and, in the case of quarks, the anticolor. There are symmetries which suggest a grouping of the leptons and quarks in generations, as in Table 1.

There are also four distinct forces associated with the interactions between the fundamental fermions. These forces are the electromagnetic force, the weak force, the strong force, and gravity. Each force is mediated by bosons, particles with integral spin. The electromagnetic force is mediated by the massless photon field,

the weak force by the three vector bosons W^\pm and Z^0 , and the strong force by eight gluons. These intermediate bosons are shown in Table 2.

There is no successful theory that describes gravity at the quantum level, but it has been hypothesized that the mediating particle should be a graviton with spin 2. The theory that describes electromagnetic interactions is Quantum Electrodynamics (QED), probably the most successful and accurate theory in physics. The weak theory was formulated in 1961 to explain nuclear decays which emitted neutrinos. In 1967, the weak and electromagnetic forces were shown, theoretically, to be manifestations of the same force, and are described in the larger Electroweak Theory. The confirming experimental evidence was obtained in 1983 with the discovery of the W and the Z bosons. The interactions between quarks and gluons are described by Quantum Chromodynamics (QCD), which was modelled after the successful QED.

Quantum Electrodynamics

Quantum Electrodynamics is a theory that evolved from the idea that a field theory should be locally gauge invariant.[1,2] It describes the interactions of electric charges as the exchange of discrete force carriers, the photons (γ). The exchange photons are virtual, meaning they can only exist within the limits of the Heisenberg Uncertainty Principle. This principle states that the uncertainty in the momentum of a system, ΔP , is related to the uncertainty in its position, ΔX by the relation $\Delta P \Delta X \leq \hbar$. When the momentum of a virtual photon approaches zero, it can travel a distance approaching infinity. This results in a spectrum of

TABLE 1
ELEMENTARY FERMIONS

	First Generation	Second Generation	Third Generation
Leptons	e	μ	τ
	ν_e	ν_μ	ν_τ
Quarks	u	c	t
	d	s	b

TABLE 2
ELEMENTARY GAUGE BOSONS

Force	Gauge Boson	Charge	Spin
E-M	γ (photon)	0	+1
Weak	W^+ (weak boson)	+1	+1
	W^-	-1	+1
	Z^0	0	+1
Strong	g_i (gluon $i = 1, \dots, 8$)	0	+1

virtual photon energies, where the photon energies are, on average, less at greater distances from the charged source. This causes the interaction strength to also decrease with distance. Experimentally, the electromagnetic force is a long range force which extends to infinity, dropping off as $1/r^2$ where r is the distance from the charged source. Thus, the notion of an electromagnetic field has been replaced by the idea of a virtual photon cloud. An electromagnetic interaction can be represented by a Feynman diagram[3] as in Figure 1. The probability amplitude for an electromagnetic process is proportional to $Z_i\sqrt{\alpha}$ for each interaction vertex. The probability for an interaction is the amplitude squared, $(Z_i\sqrt{\alpha}Z_j\sqrt{\alpha})^2$ or $Z_i^2Z_j^2\alpha^2$. The coupling constant $\alpha(\approx 1/137)$ is a measure of the strength of the interaction, and Z_i is the charge being coupled to.

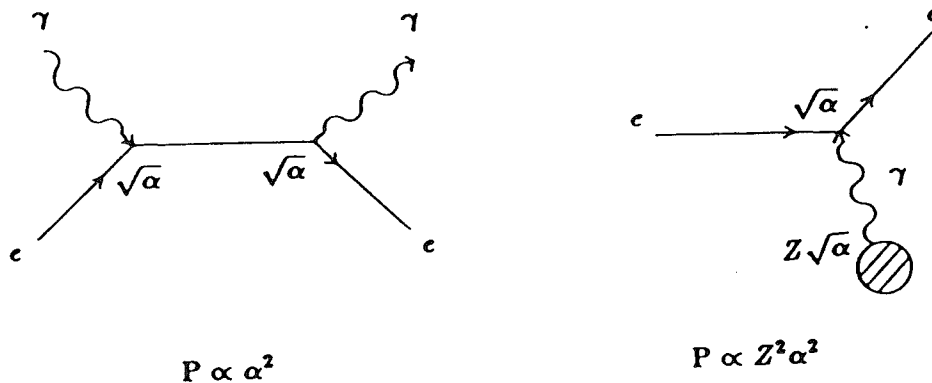


Figure 1. Feynman diagrams for EM interactions.

Quantum Chromodynamics

Quantum Chromodynamics describes the interactions between quarks. Quarks are combined to make up hadrons, which come in two types, baryons and mesons. The exchange particle which carries the strong force is called a gluon. Each quark has a quantum number called color associated with it. There are three colors, commonly labelled red, blue, and green. When quarks are combined, the resulting hadrons must be colorless. In the case of baryons, which contain three quarks, one quark must be red, one blue, and the last green. For mesons, which contain a quark and an antiquark, the quark will have a color and the antiquark will have the the appropriate anticolor in order to form a colorless particle.

An Abelian gauge field is one in which the particles do not interact among themselves, while a non-Abelian gauge field is one in which they do. The photon field is an example of an Abelian gauge field, and the gluons are an example of a non-Abelian gauge field. This represents the largest difference between QED and QCD. There are six color-changing gluons and two color-preserving gluons. A ninth gluon has no color and therefore does not participate in the strong interaction. Since gluons can couple with other gluons, the energy required to separate quarks increases at a constant rate with distance. If an attempt were made to separate two quarks, eventually enough energy would be added to the system that a quark/antiquark pair would be produced from the vacuum. This property is known as confinement and explains why a single free quark has never

been seen. Conversely, as the distance between the quarks decreases, the force between them decreases, displaying a property known as asymptotic freedom. The “running” coupling constant for the strong force, α_s , is energy dependent. Figure 2 shows Feynman diagrams for a color-changing strong interaction, and the self-coupling of gluons.

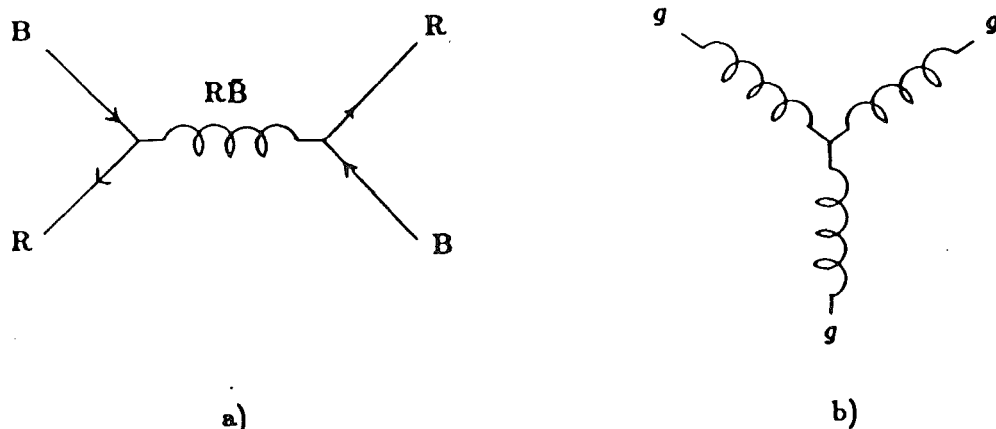


Figure 2. Feynman diagrams for QCD interactions. (a) Color changing interaction, (b) Self coupling of gluons.

Weak Theory

The weak interaction is also modelled after QED, but the exchange particles are massive, approximately 80 GeV, which restricts the interaction distance. In 1961, Sheldon Glashow published a theory based on $SU(2)$ group theory which

described weak interactions between leptons as the exchange of massive bosons.[4] These weak bosons, the W^+ , W^- , and Z^0 , can couple to a lepton/neutrino vertex and also to a quark/quark vertex. When W^+ or W^- couples to a fermion, the flavor of the fermion is changed, while the Z^0 is only involved in flavor conserving processes. The Feynman diagrams for a couple of common weak interactions are shown in Figure 3.

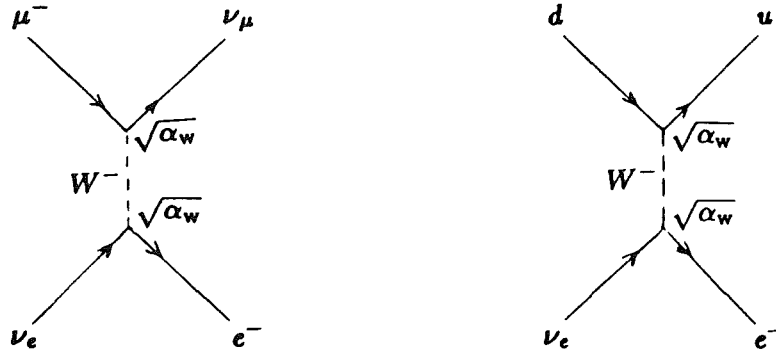


Figure 3. Feynman diagrams for weak interactions.

Electroweak Theory

In 1967, Steven Weinberg[5] and Abdus Salam[6] independently published the Electroweak Theory, showing that the weak and electromagnetic forces are manifestations of the same force. Through carefully chosen gauge transformation along with a process known as spontaneous symmetry breaking, or the the Higgs

Mechanism, the two forces are separated, leaving the photon massless and the weak bosons massive.[7] This procedure predicts a massive scalar particle, the Higgs particle, which has not been seen yet. The Electroweak Theory, using experimentally fixed parameters, was able to predict the masses of the weak bosons, and later experiments[8,9] were able to detect them. This was a beautiful confirmation of the theory and provided a convincing argument that physicists were on the right track in explaining the forces of nature. S. Glashow, S. Weinberg, and A. Salam shared the Nobel Prize in 1979 for the Electroweak Theory, and in 1984, C. Rubbia and S. Van de Meer shared the Nobel Prize for the discoveries of the weak bosons, which gives testament to the importance of these recent advances in particle physics.

Future Goals

Physicists are trying to develop Grand Unified Theories (GUTs) which are envisioned to show that the weak, strong, and electromagnetic forces are manifestations of a single force, just as the Electroweak Theory did with the electromagnetic and weak forces. A theory which would encompass the effects of gravity is considered the ultimate accomplishment. The unification energy for GUTs is expected to be $\simeq 10^{15}\text{GeV}$, and $\simeq 10^{19}\text{GeV}$ (the Planck mass) for the inclusion of gravity. These are energies that occurred moments after the Big Bang, the creation of the universe.

A theory must be verified experimentally before it is widely accepted as valid. Physicists use large particle accelerators to study elementary particles. The largest

accelerator under consideration to be built is the Superconducting Supercollider (SSC). If built, it will be able to produce collision energies of 40,000 GeV. While this will be far below the unification energies mentioned above, tests can be made of lower energy predictions from competing theories. Also, the possibility of unexpected discoveries cannot be overlooked.

When the ultimate theory is developed and tested, it should explain the creation and evolution of the universe, answering many questions including those yet to be asked.

CHAPTER II

THE PHYSICS OF CHARM

Prediction of Charm

In 1958, R. P. Feynman and M. Gell-Mann tried to build a framework for the weak interaction which would be consistent with the observed nonconservation of parity.[10] Since neutrinos only occur in left handed helicity states, they grouped the leptons into left handed doublets,

$$\begin{pmatrix} \nu_e \\ e \end{pmatrix}_L, \begin{pmatrix} \nu_\mu \\ \mu \end{pmatrix}_L, \quad (1)$$

the third generation being unknown at the time. The weak force couples only to the left handed states, and parity is not conserved. This grouping has been retained in later theories.

In order to explain the experimentally observed suppression of strangeness changing decays, relative to strangeness conserving decays, N. Cabbibo suggested that the weak eigenstates were linear combinations of the mass eigenstates.[11] The mass eigenstates have been identified as quarks, and following Cabbibo's prescription, the u , d , and s quarks have been grouped into a rotated left handed isospin doublet, and a left handed isospin singlet, as in Equation (2),

$$N_L \equiv \begin{pmatrix} u \\ d' = d\cos\theta_c + s\sin\theta_c \end{pmatrix}_L, \quad (s' = s\cos\theta_c - d\sin\theta_c)_L, \quad (2)$$

where θ_c is the Cabbibo angle, $\theta_c \approx .26$ rad. With this representation, the weak decays in which the d or s quark emitted a W^- and become a u quark were described well, the calculated decay rates agreeing with experiment. A discrepancy occurred when the neutral weak current, which would involve an s quark changing to a d quark with the emission of a Z^0 , was considered.

The Z^0 boson is coupled to the electromagnetic current, and to the flavor current of Equation (3).

$$\begin{aligned} \bar{N}_L \tau_3 \gamma_\mu N_L = & \bar{u}_L \gamma_\mu u_L - \cos^2 \theta_c \bar{d}_L \gamma_\mu d_L - \sin^2 \theta_c \bar{s}_L \gamma_\mu s_L \\ & - \sin \theta_c \cos \theta_c (\bar{d}_L \gamma_\mu s_L + \bar{s}_L \gamma_\mu d_L) \end{aligned} \quad (3)$$

The terms proportional to $\sin \theta_c \cos \theta_c$ are the strangeness changing neutral currents which allow the mixing between the s and d quarks. Experimentally, the neutral current processes which change strangeness are highly suppressed. The resolution to this problem was submitted by S. Glashow, J. Iliopoulos, and L. Maiani in 1970, and is known as the GIM model.[12] A fourth quark was proposed which would be combined with the s' quark to form an isodoublet of the form:

$$\begin{pmatrix} c \\ s' = -d \sin \theta_c + s \cos \theta_c \end{pmatrix}_L.$$

With this change, the currents $+\sin \theta_c \cos \theta_c (\bar{d}_L \gamma_\mu s_L + \bar{s}_L \gamma_\mu d_L)$ are added to Equation (3), exactly cancelling the strangeness changing neutral currents from the interactions involving the Z^0 . The only neutral process which changes strangeness is

not from the exchange of a Z^0 , but from higher order interactions in which a W^+ and W^- are both exchanged, other decay modes being more favorable. Embedded in the GIM model was the first theoretical prediction of the existence of the charm quark.

Observation of Charm

The first indirect evidence for the existence of charm came from the measurement of the ratio of cross sections for e^+e^- annihilation producing hadrons and producing a $\mu^+\mu^-$ pair. In 1973, a measurement of this ratio, at the Cambridge Electron Accelerator at a center of mass energy of 4 GeV, yielded a value of $R = 4.7 \pm 1.1$. [13] In 1974, again at the CEA, a measurement at $\sqrt{s} = 5$ GeV yielded $R = 6.0 \pm 1.5$. [14] These values were much higher than standard value of $R \approx 2$, suggesting the existence of a new heavy quark. Equation (4) shows the formula for calculating R .

$$R \equiv \frac{\sigma(e^+e^- \rightarrow \text{hadrons})}{\sigma(e^+e^- \rightarrow \mu^+\mu^-)} = 3 \sum_q e_q^2 \quad (4)$$

The summation is over the number of quarks, e_q being the electric charge of each quark. The factor of three is introduced because there are three possible colors for each quark. Below the energy threshold for charm production, summing over the u , d , and s quarks gives the value $R = \frac{2}{3} - \frac{1}{3} + \frac{2}{3} = 2$. With the inclusion of the charm quark, $R = 3.3$.

Strong experimental evidence for the existence of the charm quark came in 1974, with the simultaneous observations of a mass resonance at 3.1 GeV in an

e^+e^- mass plot produced from $P + Be \rightarrow e^+e^- + X$ at the Brookhaven National Laboratory[15] and a sharp increase in the cross section for e^+e^- annihilation at the Stanford Linear Accelerator.[16] The BNL team named this new particle the J/ψ , while the SLAC team named it the ψ . Due to the high mass and low spin of the J/ψ meson, as it is now called, it was interpreted as the $s=1$ ground state of a bound heavy quark system ($\bar{c}c$), rather than an excited state of lighter quarks.

Two years later, in 1976, the D^0 [17] and D^\pm [18] mesons were seen at SLAC. These discoveries provided the best evidence for the existence of the charm quark, since each meson contained a single charm quark coupled with one of the lighter quarks. An entire spectrum of charm particles is now known to exist. Tables 3 through 6 show the ground state and first angular momentum states of the mesons and baryons which contain c quarks. There exist higher angular momentum states for each quark combination, one of which is the D^* .

Total Charm Hadroproduction Cross Sections

Physicists have been studying the total charm cross sections in hadronic collisions for ten years, yet there is still controversy over the interpretation of the data.

Many experiments have used heavy nuclear targets, such as Fe, Be, Cu, and W. In order to compare the results from these different experiments, the calculated cross sections are scaled to the cross section of a proton target, as in Equation (5),

$$\sigma(A) = \sigma(p)A^\alpha \quad (5)$$

TABLE 3
 CHARMED $J^P = 0^-$ MESONS

Particle	Quark Content
D^0/\bar{D}^0	$\bar{u}c/\bar{c}u$
D^+/D^-	$\bar{d}c/\bar{c}d$
D_s^+/D_s^-	$\bar{s}c/\bar{c}s$
η_c	$\bar{c}c$

TABLE 4
 CHARMED $J^P = 1^-$ MESONS

Particle	Quark Content
D^{*0}/\bar{D}^{*0}	$\bar{u}c/\bar{c}u$
D^{*+}/D^{*-}	$\bar{d}c/\bar{c}d$
D_s^{*+}/D_s^{*-}	$\bar{s}c/\bar{c}s$
J/ψ	$\bar{c}c$

TABLE 5
 CHARMED $J^P = \frac{1}{2}^+$ BARYONS

Particle	Quark Content
Λ_c^+	cud
Σ_c^{++}	cuu
Σ_c^+	cud
Σ_c^0	cdd
Ξ_c^+	csu
Ξ_c^0	csd
Ω_c^0	css
Ξ_{cc}^{++}	ccu
Ξ_{cc}^+	ccd
Ω_{cc}^+	ccs

TABLE 6
 CHARMED $J^P = \frac{3}{2}^+$ BARYONS

Particle	Quark Content
Σ_c^{++}	<i>cuu</i>
Σ_c^+	<i>cud</i>
Σ_c^0	<i>cdd</i>
Ξ_c^+	<i>csu</i>
Ξ_c^0	<i>csd</i>
Ω_c^0	<i>css</i>
Ξ_{cc}^{++}	<i>ccu</i>
Ξ_{cc}^+	<i>ccd</i>
Ω_{cc}^+	<i>ccs</i>
Ω_{ccc}^{++}	<i>ccc</i>

where $\sigma(A)$ is the cross section using a target of atomic number A , $\sigma(p)$ is the cross section of a proton target, and α is the scaling parameter. Many experiments attempted a measurement of α , with varying degrees of success. Some have reported a dependence on the variable x_F ($x_F = p_{\parallel}/p_{\parallel max}$ in c.m.s.), others a dependence on \sqrt{s} , but there is general agreement that α lies between .7 and 1.

Many experiments have searched for peaks in invariant mass plots, which often resulted in large combinatorial backgrounds due to high charged track multiplicities. Others measured exclusive decay modes, and the resulting total cross section was highly dependent on branching ratios that were not well known. Table 7 lists some of the proton beam experiments that were concerned with charm production. This table was compiled by Tavernier[19] with data extracted from the original papers. He calculated the total charm pair production cross sections from the available data when the authors did not, with the assumptions that the cross section varied linearly with A , ($\alpha = 1$), and $\sigma(c\bar{c}) \approx \frac{1}{2}\sigma(pp \rightarrow D/\bar{D} + X)$. There may be an additional $\sim 20\%$ correction from D_s and Λ_c production. Previous calculations were corrected using updated branching ratios when appropriate.

It can be seen in Table 7 that the cross section in the energy range between $\sqrt{s} = 26-27$ is fairly stable at $\sigma \sim 15 \mu\text{b}$ with the variation probably due to the uncertainty in scaling with the atomic number. This statement can be supported by looking at how the cross sections vary if $\alpha = 1$, as in the table, is changed to $\alpha = .72$. The cross section from E595[20] would increase to ~ 34.9 , from HOBC[21] σ would increase to ~ 55 , from BEBC[22] σ would increase to ~ 54 ,

TABLE 7
TOTAL CHARM PARTICLE PAIR PRODUCTION
CROSS SECTIONS IN PROTON-NUCLEON INTERACTIONS

Experiment	\sqrt{s} (GeV)	Target	$\sigma(c\bar{c})$ (μb)	Comment
E595	26	Fe	$11.3 \pm 1.1 \pm 1.8$	FNAL-CCFRS collaboration; prompt 1μ $E_\mu > 20$ GeV; $n = 5$; $x > 0.3$; errors are statistical and systematic
NA16	26	H ₂	$15^{+8.2}_{-4.6}$	LEBC-EHS collaboration; D/\bar{D} only; $x_F > 0$
HOBC	26	C ₃ F ₈	$23^{+10.0}_{-7.7}$	1μ trigger $E_\mu > 6$ GeV; $x_F > 0$
BEBC	27	Cu	17 ± 4	CERN-CDHS collaboration; ν -dump; $E_\nu > 20$ GeV; $n = 3-5$; $\langle x \rangle \approx 0.8$
E613	27	W	$15.5 \pm 0.8 \pm 2.3$	FNAL ν -beam dump; $n = 4$, $E_\nu > 20$ GeV; $\langle x \rangle \approx 0.45$
CHARM	27	Cu	$15.5 \pm 2.6 \pm 1.2$	CERN ν -beam dump; $E_\nu > 20$ GeV; $n = 4$; $\langle x \rangle \approx 0.8$
NA27	27	H ₂	15.1 ± 1.7	LEBC-EHS collaboration; D/\bar{D} only; $x_F > 0$
R416	63	p	150-450	SFM/ISR; c trigger and effective mass combinations $\Lambda_c(Kp\pi)$ and $D(K\pi\pi)$
R422	62	p	129 ± 75	CBF collaboration, SFM/ISR; effective mass combination $\Lambda_c(Kp\pi)$ only
R608	53-62	p	~ 100	ISR; Λ_c effective mass combinations; $n = 0$; $x_F > 0.75$
R702	53-62	p	70 ± 36	ISR; observation of $c\mu$ pairs with opposite sign
R702	53-62	p	73 ± 21	ISR; observation of e^+e^- pairs
$\mu^+\mu^-$	63	p	< 100	ISR; analysis of $\mu^+\mu^-$ pairs for charm
c/π	53-63	p	< 300	ISR; reanalysis of all c/π data

from E613[23-25] σ would increase to ~ 60 , and from CHARM[26] σ would increase to ~ 50 . NA16[27] and NA27[28] were unique with their hydrogen targets in that they needed no atomic number corrections. Also, they had good acceptance for the entire $x_F > 0$ region.

In the energy range $\sqrt{s}=53-63$ GeV, the situation is entirely different. All experiments in this range were conducted at the CERN Intersecting Storage Ring (ISR), which is a proton-proton colliding beam facility. Spectrometer acceptance for those experiments which relied on effective mass combinations was restricted to high p_{\parallel} events while the experiments looking at lepton pair production had good acceptance only for leptons with high p_{\perp} . Also, the decays took place before any particles entered the spectrometer, resulting in poor vertex reconstruction. There are large variations in the cross sections calculated using these data, and some of the cross sections are very large. These problems were not ignored by the experimenters at CERN. The result from R416[29] of $\sigma = 150 - 450 \mu\text{b}$ listed in Table 7 came from a re-analysis of data which originally reported a cross section of $\sigma \sim 650 \mu\text{b}$. [30,31] Experiment R422[32], which obtained a cross section of $\sigma \sim 129 \mu\text{b}$, was a repeat of experiment R415, which reported a cross section of $\sigma \sim 650 \mu\text{b}$. [33-35] Lastly, experiment R608[36], which determined the cross section to be $\sigma \sim 100 \mu\text{b}$, was a repeat of experiment R603, which found a cross section of $\sigma \sim 1400 \mu\text{b}$. [37]

Further argument that the values from the ISR groups are suspect lies in the comparison of the cross sections found from the experiments which used effec-

tive mass combinations for their analyses and those which relied on the detection of lepton pairs. The effective mass experiments seem to imply a cross section $\sigma > 130 \mu\text{b}$, while the leptonic experiments imply a quite different cross section $\sigma < 100 \mu\text{b}$. [38-41]

In order to clear some of the confusion about how the cross section varies with energy, an experiment was needed at an energy between the ISR energies $\sqrt{s} \sim 53 - 63 \text{ GeV}$ and the experiments conducted at energies $\sqrt{s} < 28 \text{ GeV}$. The present experiment, E743, satisfies this need by taking data at $\sqrt{s} = 38.8 \text{ GeV}$. E743 also solves some of the other problems associated with the hadroproduction of charm, which will be discussed in a later chapter.

Differential Charm Hadroproduction Cross Sections

Experimentally it has been found that, on average, a final-state particle from a hadron-hadron collision, which contains one of the original valence quarks, tends to be produced with large x_F . A final-state particle lacking an original valence quark tends to be produced at small x_F . Models have been proposed to simply explain this phenomenon. Gunion[42] proposed a model based on simple QCD arguments which argues that the inclusive cross section should be described as $(1 - |x_F|)^n$. While this simplistic model is obviously not complete, it is still useful to parametrize the momentum dependence of charm hadroproduction by calculating the differential cross section, which is of the form:

$$\frac{d^2\sigma}{dx_F dp_{\perp}^2} \sim (1 - |x_F|)^n e^{-bp_{\perp}^2}, \quad (6)$$

where $x_F = (p_{\parallel}/p_{\parallel max}) \simeq 2p_{\parallel}/\sqrt{s}$. In the center of mass frame, p_{\parallel} is the momentum component longitudinal to the beam direction, and p_{\perp} is the momentum component perpendicular to the beam direction.

By determining the values of n and b experimentally, comparisons can be made to values calculated from various QCD models of hadroproduction. Table 8 shows the results from fits of the differential cross sections from some earlier experiments. It can be seen that there is good agreement concerning the p_{\perp} dependence of the cross section, each experiment reporting a value $b \approx 1 \text{ (GeV/c)}^{-2}$. There is less agreement concerning the x_F dependence. The A dependence of the cross section may have influenced the value from E595, and it should be noted that NA16 suffered from low statistics. There are no values of n and b listed from the ISR experiments because they were not measured, but had to be assumed in order to calculate a total cross section.

TABLE 8
PREVIOUS RESULTS OF P_{\perp} AND X_F DEPENDENCE
IN D/\bar{D} HADROPRODUCTION

Experiment	Target	$\sqrt{s}\text{GeV}$	$b(\text{GeV/c})^{-2}$	n
E595	Fe	26	1.0 ± 0.2	6.0 ± 0.8
NA16	p	26	$1.1 \pm .03$	1.8 ± 0.8
NA27	p	27	1.0 ± 0.1	4.9 ± 0.5

QCD Hadroproduction Models

In order to test and revise our understanding of QCD processes, it is important to construct models which will predict measurable quantities. The correctness of any model will be judged by a comparison of its predictions with experimental results. Three of the models proposed to explain the observed total and differential cross sections are the Fusion Model, the Flavor Excitation Model, and the Intrinsic Charm Model. While the Fusion Model seems to agree with experimental results at lower energies, the Flavor Excitation Model and Intrinsic Charm Model were invoked to describe the large cross sections and charm production at large x_F found in the ISR data.

The Fusion Model

The Fusion Model is a perturbative QCD model which states that the cross section for producing heavy quark pairs should be the sum of the cross sections for producing these pairs from the interactions between quarks and gluons within the colliding hadrons. For a collision between two hadrons A and B, the cross section for heavy quark pair production is then given by

$$\sigma_{\bar{c}c}(s) = \sum_{ij} \int dx_i dx_j G_i^A(x_i) G_j^B(x_j) \hat{\sigma}(\hat{s}). \quad (7)$$

In this formula, $\hat{\sigma}(\hat{s})$ is the cross section for the subprocess $i + j \rightarrow \bar{Q}Q + \text{anything}$, where i and j represent individual quarks and gluons, and \hat{s} is the square of the center of mass energy of this subprocess. $G_i^A(x_i)$ is the probability of finding a quark or gluon i with a fraction x_i of the momentum in hadron A.

The two most important subprocesses are gluon fusion ($gg \rightarrow \bar{Q}Q$) and quark antiquark annihilation ($\bar{q}q \rightarrow \bar{Q}Q$). It has been shown[43] that this expression will be valid if the created quarks are massive enough, but it is left to experiments to determine whether the charm quark is sufficiently massive. The Feynman diagrams for the first order processes in the perturbation expansion are shown in Figure 4.

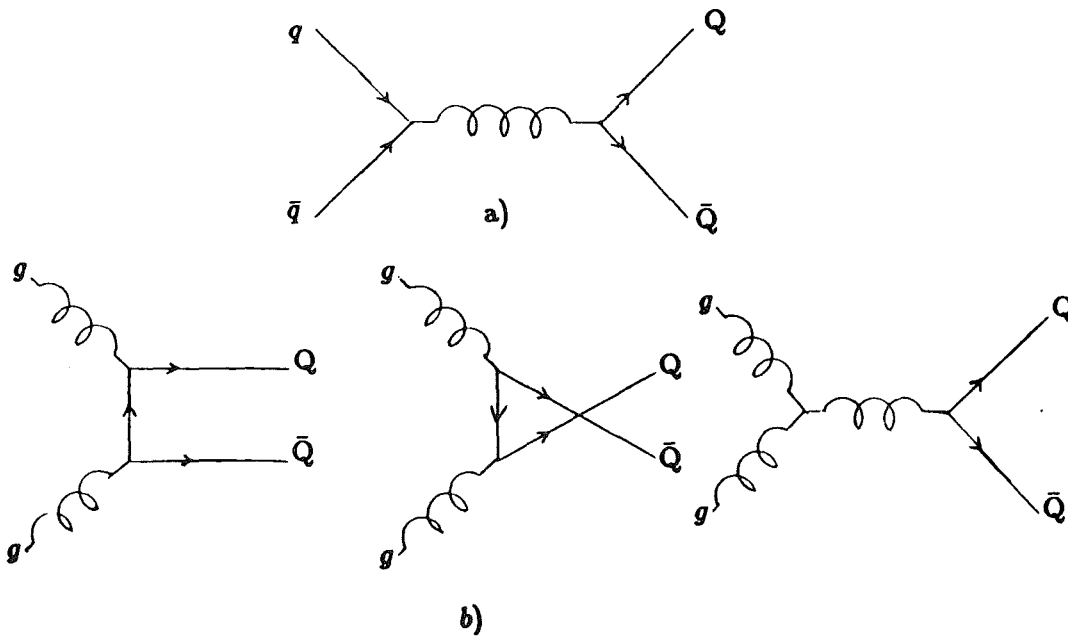


Figure 4. Feynman diagrams for a)quark-antiquark annihilation and b)gluon fusion.

There are a number of uncertainties when trying to calculate numerical quantities from the Fusion Model. One problem is that the charm quark must be assigned a mass, which is difficult to do since quarks exist only in bound states. It is generally accepted that the charm quark mass is in the range $1 \text{ GeV} \leq m_c \leq 2 \text{ GeV}$, but changing m_c from 1.2 to 1.8 GeV changes the calculated cross section by an order of magnitude. Another problem results from uncertainties in the quark and gluon structure functions. While it is known that gluon fusion dominates heavy quark production at high energies, the gluon distribution function is less well known than the quark distribution functions. Cudell *et al.*[44] performed calculations using different structure functions and found that the cross section can differ by a factor of two.

Most of these problems can be overcome by looking at the ratios of cross sections calculated using the same input parameters. Cudell *et al.* also performed this calculation which gave the value:

$$\frac{\sigma(\sqrt{s} = 38.3, \text{ E743 energy})}{\sigma(\sqrt{s} = 27.4, \text{ NA27 energy})} < 2. \quad (8)$$

Other general predictions from the Fusion Model are that heavy flavors should be produced centrally, near $x_F = 0$, and that p_\perp should be on the order of the heavy quark mass.

The Flavor Excitation Model

The Flavor Excitation Model was proposed by Combridge to explain the large cross sections and charm production at large x_F found in the ISR data.[45] In

this model, a charm quark in the quark sea of the target hadron is excited by the interaction with a gluon from the beam hadron. The Feynman diagrams for these interactions are shown in Figure 5.

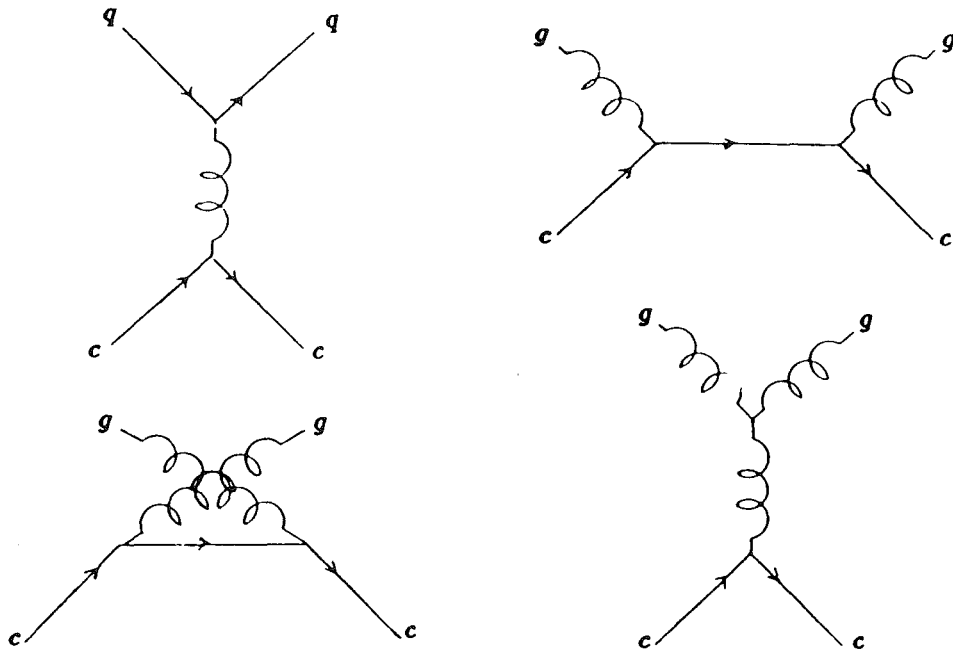


Figure 5. Feynman diagrams for flavor excitation.

The contribution to the cross section is finite since there is a cutoff for the exchange of momentum between the beam quark and target charm quark below which this interaction will not take place. The amount by which flavor excitation contributes to the total charm production is very dependent on the value of this cutoff. Combridge showed that if the cutoff value was equal to the mass of the charm quark, the contribution to the cross section would be larger and rise faster

with energy than the contributions from quark and gluon fusion. It was pointed out later that non-central production occurs naturally using this framework.[46] Odorico made detailed calculations which showed that the cutoff parameter governed the average p_{\perp} value.[47] By using experimental p_{\perp} distributions, he was able to fix the cutoff value, therefore removing some of the arbitrariness of the calculations. This approach seemed to reproduce the data. Doubts about the Flavor Excitation Model were a result of an argument that the only relevant parts of flavor excitation were actually higher order corrections to quark fusion diagrams.[48] Ellis explicitly calculated the α_s^3 contributions of flavor excitation and concluded they were indeed part of the higher order corrections to fusion or negligible.[49]

The Intrinsic Charm Model

The Intrinsic Charm Model describes a proton as consisting of a combination of particle states, one being $|uudc\bar{c}\rangle$. In this description, a proton already has a charm quark and antiquark in it, and since they are massive quarks, they carry a large fraction of the intrinsic momentum of the proton. This model predicts that most charm particles should be produced with large values of x_F . It has been shown that for sufficiently heavy quarks intrinsic charm cannot make large contributions.[50] Also, the predictions of this model conflict with data obtained from photoproduction and neutrino production of charm.[51] The implication is that there is no reason to consider intrinsic charm while dealing with the hadroproduction of charm.

Charm Decays

The charm quark decays weakly with the emission of a W^+ boson. There are three different processes through which this decay can take place: the spectator process, the annihilation process, and the exchange process. In the spectator process, the charm quark is the the only quark in the charmed hadron which partakes in the process, the others being simply spectators. In the annihilation process, a charmed meson decays when the charm quark and the bound antiquark annihilate, producing a W^+ . In the exchange process, the charm quark emits a W^+ boson which is immediately absorbed by one of the other quarks or antiquarks in the hadron. The spectator decays can be seen in Figure 6, while the non-spectator diagrams can be seen in Figure 7. In these figures, the Cabbibo favored decays ($\propto \cos\theta$) and the Cabbibo suppressed decays ($\propto \sin\theta$) are indicated.

The D^* Mesons

The D^* mesons are first excited angular momentum states($J=1$) of the D mesons. In 1976, the first indication of the D^{*+} was observed in the recoil spectrum of the D^0 . [52] Later experiments studied the $D^{*\pm}$, and D^0/\bar{D}^0 particles in more detail, determining their decay modes and branching ratios.[53,54] These values are listed in Table 9.

The D and D^* mesons both have $1/2$ unit of isospin and have approximately the same mass ($\Delta m \approx 140\text{MeV}$), which means their production characteristics should be very similar. The biggest difference between the two is their angular momenta. The D and D^* have total angular momenta zero and one, respectively.

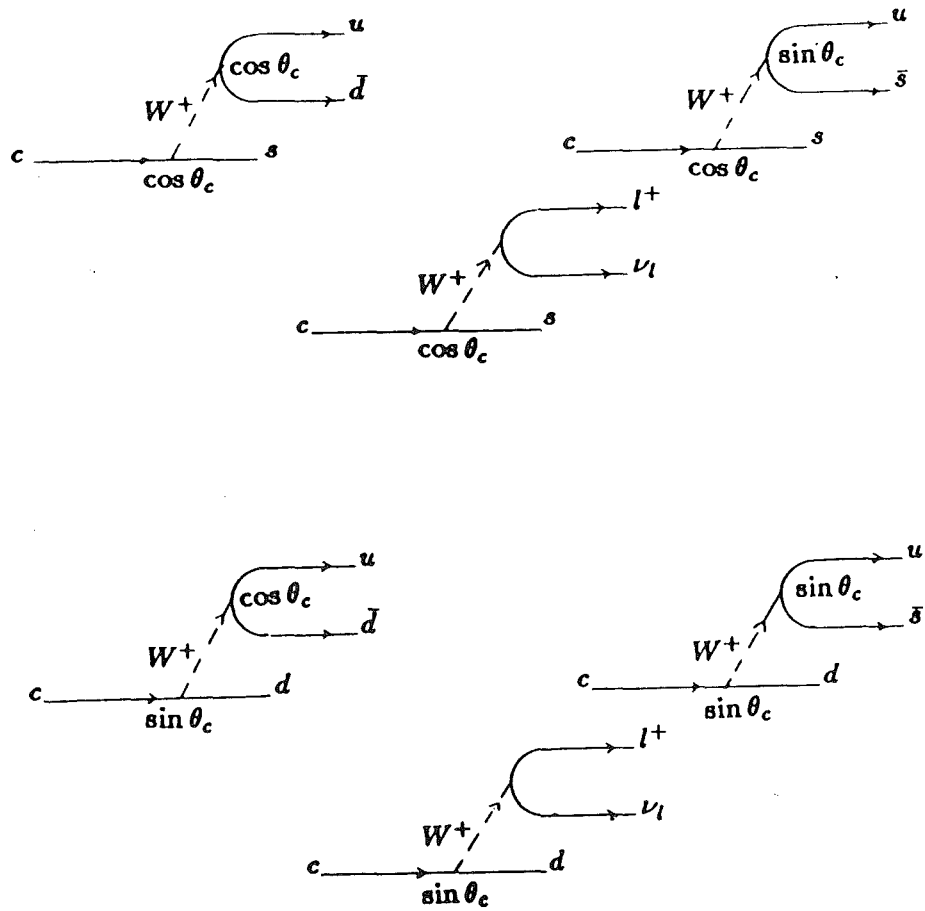
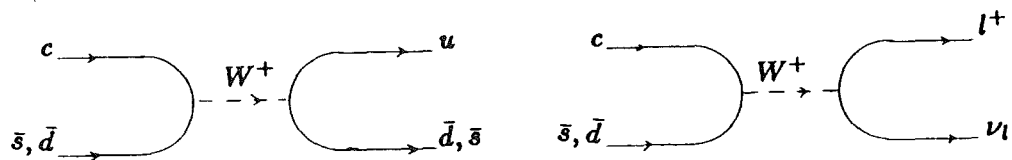
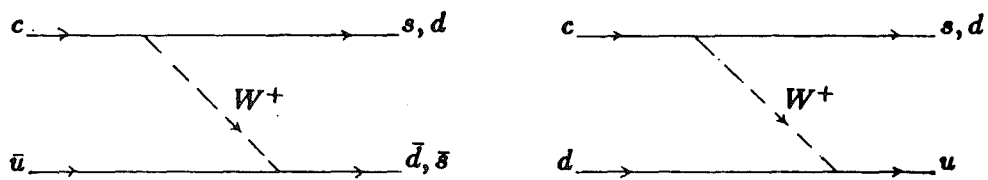


Figure 6. Quark flow diagrams showing spectator decays of the charm quark



Annihilation Processes



Exchange Processes

Figure 7. Quark flow diagrams showing non-spectator decays of the charm quark.

TABLE 9
 D^* DECAY PROPERTIES

Meson	Decay Mode	Branching Ratio(%)
D^{*+}	$D^0\pi^+$	49 ± 8
	$D^+\pi^0$	34 ± 7
	$D^+\gamma$	17 ± 11
D^{*0}	$D^0\pi^0$	51.5 ± 7.6
	$D^0\gamma$	48.5 ± 7.6

One would assume, from simple spin counting, that the D^* would then be produced at three times the frequency of the D . Since the D^* decays to the D , an experiment should find the number of final D meson states dominated by D^* production. Spin counting yields the prediction that the ratio of observed cross sections $\sigma(D + \bar{D})/\sigma(D^* + \bar{D}^*) = 1.33$. In agreement with this prediction was a measurement which yielded the value $1.1 \pm .4$. [55] One final assumption is that D^0/\bar{D}^0 and D^\pm direct production takes place at the same rate. This is a good approximation for hadroproduction at large energies, where light quarks can be readily created.

We can now make predictions concerning the observed D and D^* final states. For convenience, D^0 and D^{*0} will represent the particle and antiparticle states. The subscript t will indicate an observed total cross section, while the subscript

d will indicate a direct production cross section. As an example, the following calculation illustrates the type of prediction which can be experimentally verified:

$$\begin{aligned}
 R_1 &= \frac{\sigma(D^{*\pm} \rightarrow D^0 \pi^\pm)}{\sigma(D^0)_t} \\
 &= \frac{\sigma(D^{*\pm} \rightarrow D^0 \pi^\pm)}{\sigma(D^0)_d + \sigma(D^{*\pm} \rightarrow D^0 \pi^\pm) + \sigma(D^{*0} \rightarrow D^0 X)} \\
 &= \frac{3 \cdot B(D^{*\pm} \rightarrow D^0 \pi^\pm) \cdot \sigma(D^0)_d}{\sigma(D^0)_d \cdot [1 + 3 \cdot B(D^{*\pm} \rightarrow D^0 \pi^\pm) + 3]} \\
 &= .27 \pm .05,
 \end{aligned} \tag{9}$$

where the error is due to the errors on the D^* branching ratios. In Table 10, predicted values and experimental results from NA27[56] are displayed and agree within errors.

TABLE 10
PRODUCTION OF D AND D^* MESONS

Quantity	Experimental Value	Predicted Value
$\frac{\sigma(D^{*\pm} \rightarrow D^0 \pi^\pm)}{\sigma(D^0)}$	$0.24^{+0.09}_{-0.06}$	0.27 ± 0.05
$\frac{\sigma(D^{*0} \rightarrow D^0 \pi^0)}{\sigma(D^0)}$	0.40 ± 0.13	0.28 ± 0.04
$\frac{\sigma(D^0 \text{ from } D^*)}{\sigma(D^0)}$	0.98 ± 0.28	0.82 ± 0.06
$\frac{\sigma(D^\pm \text{ from } D^*)}{\sigma(D^\pm)}$	$0.44^{+0.25}_{-0.21}$	0.61 ± 0.18

CHAPTER III

EXPERIMENTAL APPARATUS AND DATA AQUISITION

Introduction

Experiment E743 was conducted in the MT beamline at Fermilab, in Batavia, Illinois (See appendix A). We used the Lexan Bubble Chamber (LEBC) filled with hydrogen as a target and high resolution vertex detector, and the Fermilab Multi-Particle Spectrometer (FMPS), with the addition of proportional tubes and extra wire chambers, for particle tracking and momentum determination. For particle identification, we used two Čerenkov detectors and a transition radiation detector (TRD). A PDP11, running MULTI, was used to read out the electronics and write our event data on magnetic tape for analysis.

The Beamline

We were supplied with 800 GeV/c protons extracted from the Fermilab Tevatron. The protons arrived in beam spills of 23-second duration with approximately 40 seconds between spills. The primary beam had an intensity of approximately 10^{11} protons per spill, but was reduced to approximately 10^5 protons per spill by the use of a 1 mm^2 pinhole and a 1.2 m long Be absorber. The intensity was

reduced in order to prevent an overabundance of beam tracks in the bubble chamber, which would have made scanning of film impossible. The beam was focused as it passed through two quadrupole magnets and three collimators. The final beam area at LEBC was 8 mm vertically and 1 mm horizontally, which was well within the focal volume of the cameras.

The Bubble Chamber

LEBC was a small, rapid cycling, hydrogen bubble chamber. The chamber body was built entirely from Lexan parts which were vacuum sealed together by a special cementing technique. Lexan is transparent to visible light and has high impact strength, even at cryogenic temperatures. Two stereoscopic views were photographed, illuminated by a pumped dye laser, with the 520 nm wavelength light being guided by two glass fibers. The two cameras were oriented such that the two views were rotated approximately 4 mrad relative to each other. The photographic volume in each view had dimensions of 109 mm along the beam, 50-55 mm in height, and a depth of 2 mm. We used 50 mm film and optics which produced a demagnification from space to film of 1.1 to 1.0. The bubble diameter of the triggered events was $23\text{ }\mu\text{m}$, which is our two-track resolution. LEBC had a maximum cycle rate of 25 Hz, but our data taking rate was limited by the camera, which had a cycle rate of 15 Hz.

As mentioned in Chapter II, LEBC was used previously in experiments NA16 and NA27 and provided the most reliable data for charm hadroproduction at energies below $\sqrt{s} < 30\text{ GeV}$. We used it at $\sqrt{s} = 38.8\text{ GeV}$ as a target and high

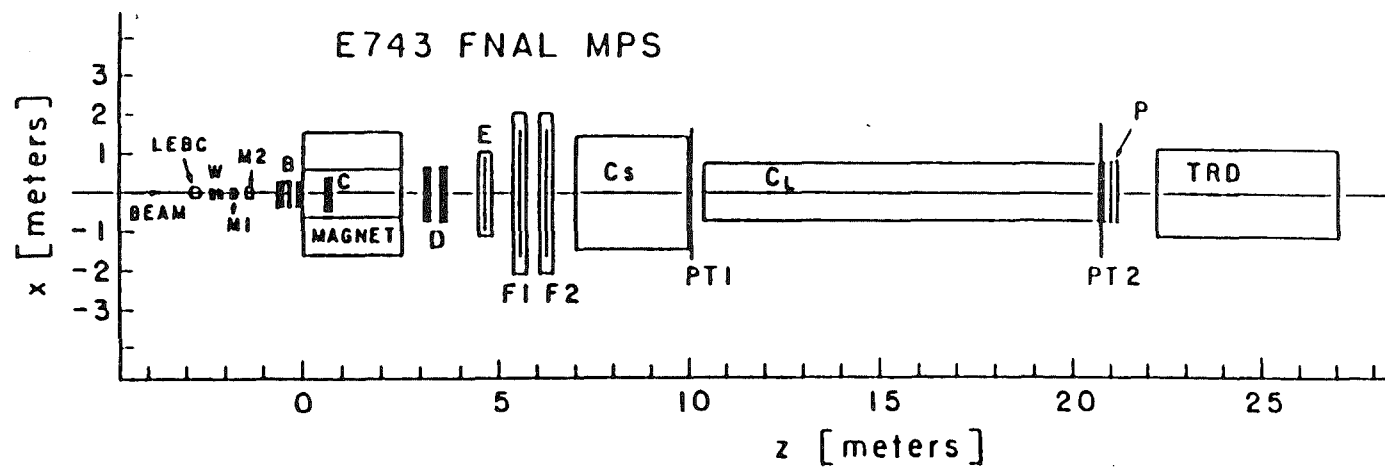
resolution vertex detector. Since LEBC was filled with liquid hydrogen, it provided a target which eliminated the need for A corrections when we calculated the charm cross section. Decays occurred inside the bubble chamber and were recorded on film. Examination of these events provided accurate interaction and decay vertex measurements. Differentiating between a secondary decay and a secondary interaction was accomplished by simple track counting. Due to conservation of charge, a neutral decay would have an even number of charged tracks leaving the decay vertex, while a charged decay would have an odd number. The photographs also allowed us to match decay tracks with their appropriate decay vertices unambiguously, a feature absent in all non-bubble chamber experiments.

The Spectrometer

The spectrometer was oriented in a right handed coordinate system with x increasing towards the west, and y increasing vertically. This placed the z coordinate increasing towards the north, downstream along the beam direction. The origin of the coordinate system was defined as the center of the front aperture of the magnet. See Figure 8 for a layout of the spectrometer.

The Magnet

The momentum analyzing magnet was a superconducting magnet which produced an average field of 1.6 Tesla and imparted a transverse momentum of approximately 700 MeV/c. It had an aperture of 1.23 m horizontally (the bend plane), 0.84 m vertically, and was 2.54 m long. Most particles which were in the acceptance



Top View

Figure 8. The E743 spectrometer configuration.

of the magnet and had momenta above 3 GeV/c would traverse the magnet and enter the downstream section of the spectrometer. They could then be momentum analyzed.

Tracking Chambers

The wire chambers upstream of the bubble chamber, were proportional wire chambers (PWCs), which were used to reconstruct the incoming beam. These chambers consisted of three x planes, one y plane, three u planes, and three v planes. The terms x, y, u, and v refer to the coordinates which were measured, the u and v being slant coordinates. Between LEBC and the mid-magnet plane, were PWCs consisting of six x planes, six y planes, two u planes, and one v plane. Downstream of the magnet there were ten PWC planes, four x planes, four y planes, two u planes, and two v planes. In addition, there were two drift chambers, which supplied a total of four x planes, four u planes, and four v planes. Finally, there were four planes of proportional tubes downstream, two x planes and two y planes, each supplying an associated charge division coordinate. Characteristics of the wire chambers are displayed in Table 11.

Particle Identification

There were three particle identification detectors downstream of the magnet. Č-short was a Čerenkov radiation detector filled with nitrogen at atmospheric pressure. It gave light at threshold momenta for $\pi/K/p$ of 5.7/20/38 GeV/c. Downstream of Č-short was Č-long, another Čerenkov radiation detector. Č-long was

TABLE 11
E743 TRACKING CHAMBER PARAMETERS

Plane	Z Position (mm)	X Aperture (mm)	Y Aperture (mm)	Wires	Spacing (mm)	Resolution (mm)
WX1	-2535.3	80.0	80.0	160	0.500	0.144
WX2	-2479.1	80.0	80.0	160	0.500	0.144
WY1	-2442.3	80.0	80.0	160	0.500	0.144
BX1	-739.8	768.0	630.0	384	2.000	0.577
BV	-630.2	768.0	630.0	416	1.954	0.564
BY1	-564.5	768.0	630.0	224	2.000	0.577
BU	-501.1	768.0	630.0	416	1.954	0.564
BX2	-401.5	768.0	630.0	448	1.954	0.564
BY2	-322.5	768.0	630.0	320	1.954	0.564
BX3	-180.5	768.0	630.0	512	2.000	0.577
BY3	-81.9	768.0	630.0	288	2.000	0.577
CU	448.2	955.0	630.0	416	1.954	0.564
CX	609.6	955.0	630.0	512	1.954	0.564
CY	687.8	955.0	630.0	320	1.954	0.564
DX1	3013.6	1938.0	1134.0	992	1.954	0.564
DY1	3127.7	1938.0	1134.0	320	3.175	0.917
DV	3222.0	1938.0	1134.0	864	1.954	0.564
DU	3337.5	1938.0	1134.0	864	1.954	0.564
DY2	3562.8	1938.0	1134.0	320	3.175	0.917

TABLE 11-CONTINUED

Plane	Z Position (mm)	X Aperture (mm)	Y Aperture (mm)	Wires	Spacing (mm)	Resolution (mm)
DX2	3678.5	1938.0	1134.0	992	1.954	0.564
E1X	4953.8	2032.0	2032.0	800	2.540	0.733
E1Y	4971.8	2032.0	2032.0	800	2.540	0.733
E1U	4989.8	2032.0	2032.0	896	2.540	0.733
E1V	5007.8	2032.0	2032.0	896	2.540	0.733
F1U	5612.3	3353.0	1700.0	192	18.246	5.267
F1V	5631.3	3353.0	1700.0	192	18.246	5.267
F1X2	5669.3	3353.0	1700.0	176	19.050	5.499
F1X1	5650.3	3353.0	1700.0	176	19.050	5.499
F2U	6322.0	3353.0	1700.0	192	18.246	5.267
F2V	6341.0	3353.0	1700.0	192	18.246	5.267
F2X2	6360.0	3353.0	1700.0	176	19.050	5.499
F2X1	6379.0	3353.0	1700.0	176	19.050	5.499
PT1Y	10082.6	3674.0	1623.0	64	25.435	7.342
PT1X	10114.4	3674.0	1623.0	144	25.473	7.353
PT2Y	21148.5	3674.0	1623.0	64	25.446	7.346
PT2X	21180.2	3674.0	1623.0	144	25.487	7.357
PX	21983.5	1626.0	1219.0	640	2.540	0.733
PY	22000.9	1626.0	1219.0	480	2.540	0.733

filled with helium at atmospheric pressure, and had threshold momenta for $\pi/K/p$ of 17/59/112 GeV/c. Both Čerenkov detectors were run in differential mode, allowing identification even when competing hypotheses were all above threshold by predicting how much light would be produced for each mass hypothesis. The third particle identification detector was a transition radiation detector (TRD). Since a TRD is a relatively uncommon detector, its operation will be explained in more detail.

Transition radiation, in the form of tr-photons, occurs when a charged particle traverses an interface between two media with different dielectric constants. The intensity of this radiation grows with the Lorentz factor $\gamma = 1/\sqrt{1 - \beta^2}$ of the particle. This feature is advantageous as accelerators produce higher and higher energies.

The probability for a fast moving charged particle to produce a tr-photon is of the order $\alpha \sim (1/137)$, it is therefore advantageous to have many interfaces. This can be accomplished with a radiator composed of a stack of thin foils, or a radiator composed of randomly arranged fibers. In our TRD, the radiator panels were composed of randomly arranged carbon fibers, loosely packed, each fiber supplying two interfaces. There were twenty panels of radiators, each followed by a PWC to detect the tr-photons. Since the photons produced have energies of about 9 keV, the PWCs should be filled with a gas of high photoabsorption cross section. Unfortunately, the PWCs detect not only the tr-photons, but also the ionization loss of the particle as it passes through the detector gas. Since the

photoabsorption cross section increases as Z^5 and the energy deposited through ionization loss increases as Z (atomic number), a gas of high Z , such as xenon, is ideal. The gas we used was a mixture of 19% xenon, 8% methane as a quenching gas, and 73% helium. This mixture had the same density as air and minimized the bending in the mylar windows, which acted as cathodes. The entire gas system was closed, and the gas circulated through a complicated regulating and filtering system to prevent the gasses from separating, and to allow the filtering out of moisture and oxygen.

The Trigger

The event trigger in E743 was a minimum bias trigger which required a clean proton track entering LEBC, and at least three charged particles exiting the chamber. A clean track meant the proton entered LEBC within the focal plane of the cameras with no beam halo particles in coincidence. The minimum bias trigger was used in order to avoid model dependent corrections on the event sample.

The event trigger began as a pretrigger using six scintillators upstream of LEBC. A clean beam particle which would traverse LEBC within the focal volume was insured when the logical combination $T1 \cdot T2 \cdot T3 \cdot T4 \cdot \overline{(V1 \cdot V2)}$ of these scintillators was satisfied. Figure 9 shows the configuration of these scintillators.

Once the pretrigger occurred, the event trigger required three more conditions. The first condition was that the cameras were ready, which meant the film had advanced after the last picture. Secondly, the bubble chamber had to be ready. This meant that LEBC was at its pressure minimum. Lastly, an interaction was

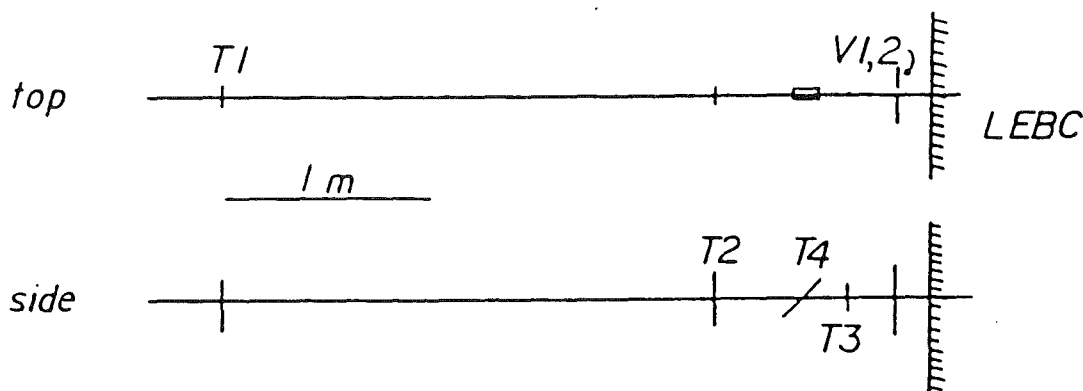


Figure 9. The E743 trigger configuration.

required in the bubble chamber. An interaction was determined to have taken place when two planes of the high resolution proportional wire chambers (WX1 and WX2), which were stationed directly behind LEBC, each detected at least three hits from charged particles. This type of trigger eliminated any event bias.

During the expansion cycle of LEBC, before minimum pressure was reached, it was desirable to prevent beam particles from entering the chamber in order to reduce confusion when scanning the film. This was accomplished with a kicker magnet in the beamline upstream of LEBC. During this sensitive expansion, the kicker magnet was supplied with current which had the effect of bending the beam trajectory away from the experimental hall.

CHAPTER IV

DATA ANALYSIS

Introduction

The E743 data-taking run lasted four months. At the end of that time we had taken approximately 1.3 million LEBC pictures and filled approximately sixty data tapes. The film was then scanned and measured while the spectrometer data were studied and the analysis software was fine tuned. Finally, the LEBC measurements and spectrometer information were combined, and each interesting event was analyzed. In order to organize and access our large data structures, we used the HYDRA data management programs developed at CERN. HYDRA allows users to place data in "banks", then define how these banks will be linked to existing banks. The end result is a data structure resembling a tree, with well defined paths for reaching each branch.

Scanning LEBC Film

The first stage in the event selection and analysis took place on the scanning table. Our film was divided among many different universities and laboratories around the world to be scanned, but the procedures were the same at each. The LEBC pictures were projected onto scanning tables, and each camera view was carefully studied. The purpose of scanning the film was to select events that were

topologically consistent with charm decays. There were three scans performed on every roll of film.

The first scan of the film was directed by a prediction program. This program used the information from wire chambers upstream from LEBC to predict where the primary beam proton would enter the bubble chamber. The job of the scanner was to first find the primary interaction and confirm that it was consistent with the prediction. This insured that the event trigger was real, not a result of stray tracks or an interaction in the entrance or exit window of LEBC. Then any secondary activity was searched for.

The second scan was directed by the first scan. Any event with a primary interaction consistent with the prediction, as determined by the first scan, was looked at again to search for secondary activity. Both of these scans noted the positions of the primary vertices and any secondary vertices as well as the topology of the secondary activity.

The different types of topologies were classified as C_n , V_n , or X_n , where $n=1, 2, 3, \dots$ was the number of charged tracks leaving a secondary vertex. The "C" denoted a secondary vertex in which a charged track entered the vertex, and "n" tracks emerged. Due to charge conservation, if "n" was odd, this was the decay of a charged particle, while if "n" was even, this represented a charged particle interacting with a proton in the hydrogen which filled the chamber. Likewise, a "V" event denoted a neutral particle either decaying into an even number of charged particles, or interacting and producing an odd number of charged particles. An

event was classified as an "X" if the secondary vertex could not be seen due to the confusion caused by tracks from the primary vertex, but some kind of secondary activity existed since there were "n" tracks that obviously did not originate from the primary vertex.

In the third scan, any event which contained some type of secondary activity, as determined by one or both of the first two scans, was studied by a physicist. At this time, the topology was confirmed or changed, and topological cuts were applied to reduce the number of non-charm decays sent to the measuring table. The secondary vertex was required to lie within the charm box, a box extending 1 mm transverse to the beam, and 4 mm along the beam from the primary vertex. This cut reduced the background from long-lived strange particles. The secondary vertex was also required to lie at least 0.5 mm from the exit window of LEBC. It was demanded that an X event have no more than one track with a decay angle greater than 150 mrad. If an event satisfied these criteria, the physicist would then carefully match secondary tracks in the two camera views using bubble size and spacing as guides. Once completed, the film was sent to one of the two measuring labs.

Measuring LEBC Film

Once an event passed the third scan, the film was sent, along with the information obtained during the scanning procedures, to one of the two measuring labs. The two measuring machines were ERASME at CERN in Geneva, Switzerland,

and ADAM & EVA at the Universite de l'Etat a Mons in Mons, Belgium. Measuring a picture meant digitizing the bubble positions and the fiducial marks so space coordinates could be assigned to the vertices and tracks. The bubble positions for each track were used in a least squares fit to a straight line. The resolution of the measuring machines was $2\text{ }\mu\text{m}$. The bubble size was $20\text{ }\mu\text{m}$ and the bubble density was 8 bubbles/mm for minimum ionizing tracks. The measuring precision for the position of the bubble centers was $2\text{ }\mu\text{m}$. When the measurements were completed, a measurement file was created in the HYDRA format containing all of the relevant measurement information.

ADAM & EVA Measuring Machine

The first step of measuring on ADAM & EVA involved a preliminary scan. Pictures were projected onto a measuring table one floor below at 25X and 40X magnification and the topology was once more confirmed. The total multiplicity of the event was also determined at this time.

The measuring was done at the 25X magnification. The scanning table was equipped with a stationary cross hairs and manual controls for moving the picture. A position on the picture was digitized and then recorded by a computer when the operator placed the position over the cross hairs and pressed a foot pedal. First, the five fiducial marks were measured. Next, the primary vertex was located and measured. The operator took extra care to locate the vertices accurately. This information then appeared on a color graphics screen. The tracks were then measured, first the incoming beam track and then the primary tracks. If possible,

the operator choose at least twenty points along the entire track length to measure. The operator would begin near the vertex or near the end of the track, whichever reduced the confusion. Once the vertex and at least one other point on the track had been measured, the computer predicted the position of the next track position to be measured and directed the measuring machine to move the film to that location. The operator could perform any necessary fine tuning with the manual film controls. Once the entire track had been measured, the information was used by the computer to perform a least squares fit to a straight line. If the fit was good ($\text{r.m.s.} \leq 3 \mu\text{m}$) the line was drawn on the display, assigned a label, and the positions with the fitted statistics were stored by the computer. If the fit was bad, the bad points ($\text{r.m.s.} \geq 6 \mu\text{m}$) were remeasured or the entire track was remeasured. Next, each secondary event (vertex and tracks) was measured. Here, each track was also labelled, as guided by the bubble matching performed earlier at the physicist edit. Note that the secondary tracks, when drawn on the display, extended beyond their associated vertex. This was used later by a physicist to determine whether a secondary track was actually associated with the primary vertex, and not a secondary vertex. The above procedure was repeated for each of the two views.

ERASME Measuring Machine

ERASME was a interactive light scan device which projected a thin beam of light, $15 \mu\text{m}$, through the film. The light intensity was measured by a photomultiplier and recorded as a function of the spot position. This information was

displayed on a color graphics monitor. The operator could position the reference cross, at which time ERASME would use an algorithm which directed a scan about this point in order to maximize the quality of the track parameters. As with ADAM & EVA, the operator could observe the track fit parameters on the monitor and could reject bad points or remeasure the track. Aside from the mechanical aspects of the two measuring machines, the measuring procedures were the same, and the results were comparable as determined by a small sample of film which was measured on both machines.

Synchronization

The bubble chamber pictures and spectrometer data were two different physical records of the events. In order to use them together, the proper MULTI record had to be found for each picture. This synchronization process went smoothly most of the time since each picture had a roll and frame number on it, which corresponded to a roll and frame number in each MULTI record. In the perfect case, the appropriate MULTI record was simply copied from a data tape. Unfortunately, this procedure was not always simple due to equipment errors during the data taking run. At times, the roll and frame numbers on the film and those on the tape did not match each other properly. In this case, painstaking measures were taken on a roll by roll basis, and occasionally on an event by event basis, in an attempt to find the proper MULTI record. The synchronization program produced a data file, which was simply the original MULTI record with the vertex measurements from LEBC written at the end. An event was considered to be

synchronized when the full track reconstruction was performed, and a significant fraction of the measured tracks were matched with tracks reconstructed from the spectrometer data.

Track Reconstruction

FLOWERS was a track finding program originally written by J. H. Goldman for the Fermilab experiment E623, and modified by J. W. Waters to accommodate our spectrometer configuration. It was used to reconstruct tracks using only the spectrometer information. FLOWERS could be run in one of three modes, a simple one receiving data over the PDP11-VAX link used for monitoring purposes while taking data, a high statistics one used for histogramming and calculating efficiencies, and a production mode for writing output used in GEOMETRY. The first mode was not used much since the track finding was not reliable enough during most of the data taking period. The second mode was quite useful in uncovering errors in the chamber readouts and fine tuning the survey information. The third mode produced the data for particle identification calibrations and for use in the full event reconstruction. The following discussion will be restricted to the production mode.

In production mode, FLOWERS was given the synchronized data files for the events, which insured that the vertex coordinates from the measurements and all of the spectrometer data were available. FLOWERS used two downstream X chambers to define an X-Z road, then searched the rest of the X chambers for hits along that road. Once an acceptable track was found, an extrapolation

was done to the mid-magnet plane. A search was then done using the upstream X chambers and the vertex coordinates. A successful match between upstream and downstream tracks in the X-Z plane was determined subject to the condition that the two tracks intersected near the mid-magnet plane. A momentum was then calculated assuming a transverse momentum kick of 697 MeV/c.

Once the X-Z projection of a track was found, an attempt was made to find the Y-Z projection. If there was a proportional tube hit on the X-Z track, the associated charge division hit was used to define a liberal Y-Z road. The Y chambers and slant chambers were then searched for hits along this road. If there was no proportional tube hit, then each of the hits in a selected slant chamber was used, along with the previously determined X coordinate, to define a Y-Z road. The search then proceeded for hits along this road. Vertical focussing of the magnet was incorporated in the search for the Y-Z projection of the track by using a table of angle and slope differences. The complete track was then refitted using all of the best hits and the individual momentum components were calculated. If the Y-Z match failed, the X-Z track was saved, but the momentum components were set to zero.

Event Reconstruction

After the measurements were done and FLOWERS found tracks in the spectrometer, GEOMETRY was used to combine this information. Matching between LEBC tracks and FMPS tracks was done globally to obtain the best set of matches. The track fitting then used all of the information available, including the magnetic

field grid. LEBC tracks which did not match spectrometer tracks or had fits which failed were candidates for track recovery.

Track Hybridization

GEOMETRY was the program which did the final track hybridization. The first step in this process was performed by the processor MAT, which constructed three-dimensional tracks in the bubble chamber from the two measured views, and matched them to tracks found by FLOWERS. Then the SFT processor refitted the track in three dimensions using the full magnetic field grid.

The matching processor, MAT, was written to find the best combination of bubble chamber tracks and tracks from FLOWERS. In effect, MAT was working with three views, two from the bubble chamber and one from the spectrometer. All possible combinations of the three views were made and quality of the match was based on how well the angles from the LEBC track, made from two views, matched the upstream angles of the track from FLOWERS. Of course, those tracks in the bubble chamber which were matched by hand remained matched, reducing the number of possible combinations. The selection of which matches were best was done globally, insuring that the best set was chosen. After the global matching was done, the ZLA processor used one more pass through MAT, extrapolating the bubble chamber tracks through the upstream chambers in order to find hits in the WX and BX chambers. A successful ZLA match resulted in better angle resolution than was provided by the bubble chamber alone.

When a suitable three-view match was found, the all-important SFT processor was called. This processor attempted a fit in three dimensions to all the wire chamber hits associated with the track found by FLOWERS and the bubble chamber measurements. SFT used the estimated momentum supplied by FLOWERS to swim the track through the magnetic field grid. In an iterative process, SFT could remove up to five hits from a track to minimize the chi-square of the fit, and determine the momentum more accurately. The error on the momentum of a hybridized track could be parametrized as $\Delta(1/p) = 1.84 \times 10^{-4} + 3.4 \times 10^{-3}(1/p)$ if it contained hits in the drift chambers, but not in the PX chamber. If it contained hits in the drift chambers and the PX chamber, the error was smaller and could be parametrized as $\Delta(1/p) = 1.32 \times 10^{-4} + 3.85 \times 10^{-3}(1/p)$. Figures 10 and 11 show the errors taken from the actual data. A fully hybridized track was one which passed through SFT without a problem. Some tracks could not be hybridized fully, resulting in an SFT failure.

Track Recovery

As would be expected, track reconstruction and hybridization was not perfectly efficient. It was sometimes beneficial to employ hand-steered track recovery techniques to help reconstruct an event.

After an event had been processed by GEOMETRY, all of the tracks could be classified as one of five types. The first type was a hybridized track, one found by FLOWERS, matched to a bubble chamber track, and processed successfully by SFT. This was the most desirable track. A second type of track was one similar

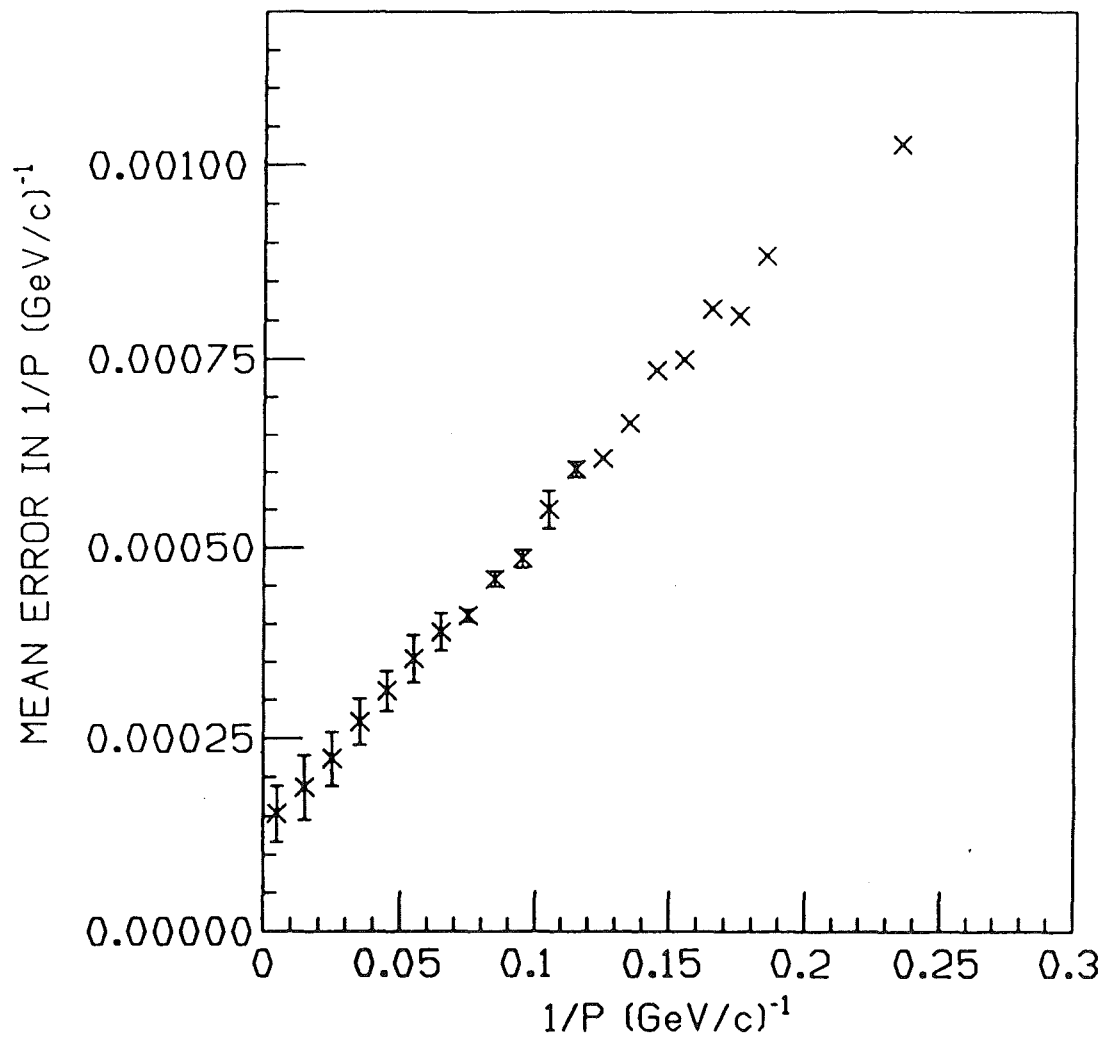


Figure 10. Mean error in $1/p$ for tracks with hits in the PX chamber.

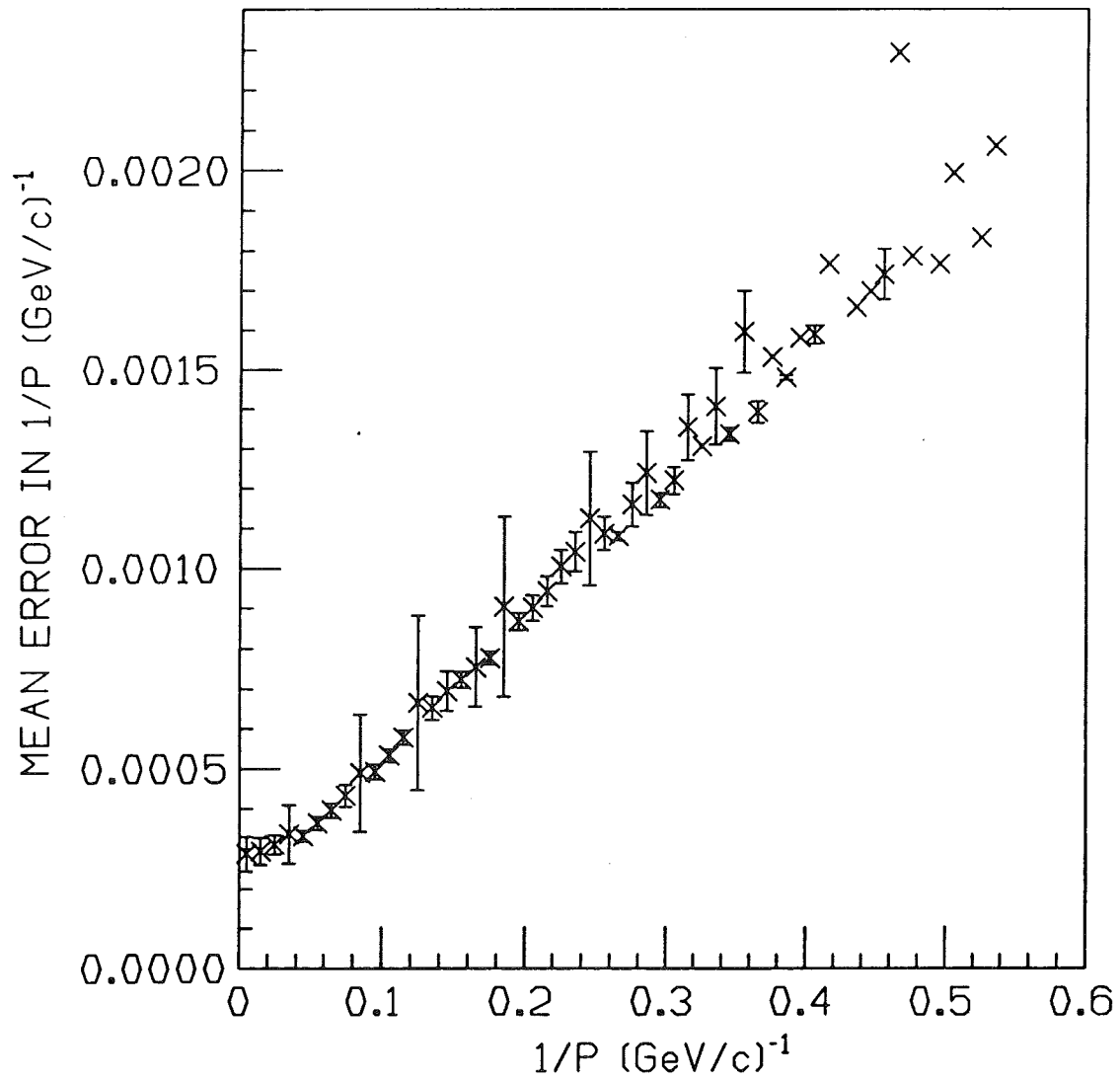


Figure 11. Mean error in $1/p$ for tracks without hits in the PX chamber.

to the previous one, except it failed in SFT. This could be caused by a number reasons, but the end result was that the match between the bubble chamber track and spectrometer track could not be trusted. A third type of track occurred when FLOWERS found a track only in the bend plane, but it was subsequently matched to a bubble chamber track and hybridized. Although a momentum estimate existed for this track from FLOWERS, the lack of a Y-Z projection caused doubts about its trustworthiness. The fourth type of track was measured in the bubble chamber, but only found upstream of the magnet by the ZLA processor discussed before. These tracks lacked any momentum determination. The final type of track was the lost track. This was a track measured in the bubble chamber, but not found at all in the spectrometer. A lost track was sometimes labelled "Out of Acceptance" if an extrapolation of the measurement in the bubble chamber was out of the W chambers, or struck the magnet. The tracks which were candidates for track recovery consisted of the SFT failures, the tracks with no Y-Z projection, the tracks found only by ZLA, and the lost tracks.

Initially, track recovery was done with E743PIX, an interactive graphics program. The tracks as measured in the bubble chamber were displayed on a graphics terminal, along with the hits in the various wire chambers (See Figure 12). There were two displays, one for the X-Z projection and one for the Y-Z projection. To construct a track, one view was displayed on the terminal. Usually the non-bend plane was chosen first. A road was defined by choosing two hits which seemed to form a track that would intersect the bubble chamber track in the middle of

the magnet. The program then searched for other hits consistent with this new road. The other view was then displayed and the process repeated. E743PIX then formed a three-dimensional track downstream, looked for hits in the slant chambers consistent with the new track, and fitted a line to all of the hits. The upstream piece of the track was then automatically constructed by extrapolating the measured track from the bubble chamber through the upstream wire chambers and searching for hits. If the upstream and downstream pieces of the track intersected within errors in the middle of the magnet, and at least one slant hit was found downstream, the new track was considered as a possible real track. The momentum was then estimated as in FLOWERS, and a formatted file was produced containing the track information. This file would then be read by GEOMETRY, which created a track bank in the HYDRA structure which looked the same as a FLOWERS track. The event was then processed as usual. Of course, if any of the requirements above were not satisfied, the track was rejected and the process continued. As it happened, many tracks would normally be constructed which passed the above criteria, and a final selection had to be made using more information.

The information came from a slightly modified version of GEOMETRY called TGRAF, which would read in one graphics track at a time, processing the event each time. The information for this track would then be dropped from the HYDRA bank before the next track was read in. This procedure gave each graphics track an equal chance of being processed. TGRAF also produced important new output. Since SFT could remove hits from a track in order to improve the fit, it was

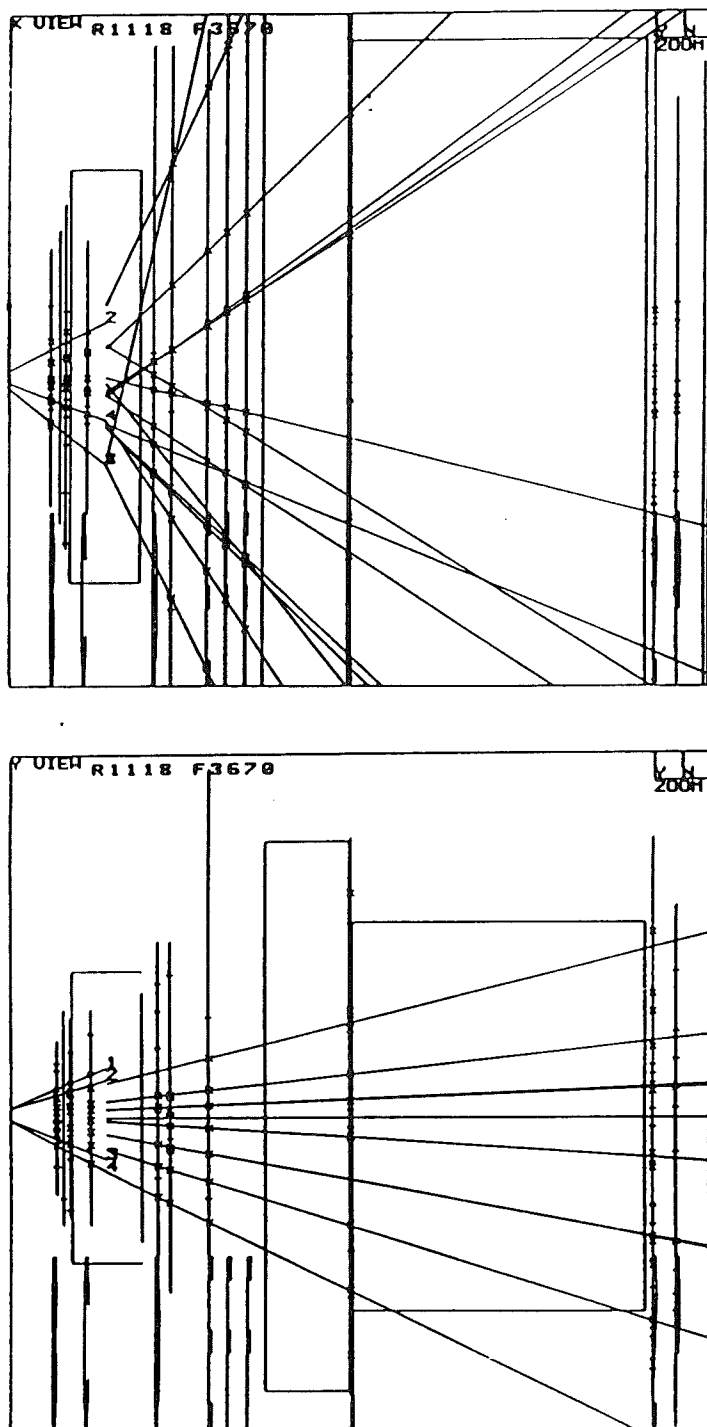


Figure 12. Example displays from E743PIX

important in judging the merits of one graphics track over another to know which hits remained on a track after SFT had finished with the fit. TGRAF supplied this information. In order for a track to be accepted as reliable, it first had to match the bubble chamber track and pass the SFT processor without failing. It must also emerge from SFT with an absolute minimum of one X chamber hit, one Y chamber hit, and one slant chamber hit remaining on the downstream piece of the track. When more than one graphics track still passed these criteria, then the best was chosen by comparing the number of hits of each kind, giving priority to slant hits, and by looking at the total fit probability as calculated by SFT.

A second procedure for reconstructing tracks was later developed. The new method was based on the GEOMETRY subroutine SWIM. SWIM, when given the charge, momentum, and upstream slope and intercept, processed the track through the magnetic field grid and provided a downstream slope and intercept for the track. With this information, it was possible to calculate a coordinate in each downstream chamber which would correspond to this track. A search, by hand, through a printout of the raw chamber hits was then conducted to select the hits that would make up this predicted track. Using these hits, a file was produced, identical in format to one produced by the graphics program. This could then be used as input to TGRAF, and the track was selected or rejected based on the same criteria as mentioned before.

The upstream slope and intercept were calculated using the vertex space coordinates along with the $\text{dip}(\lambda)$ and $\text{phi}(\phi)$ angles of the track in question. The

charge and momentum were the parameters that could be easily varied to produce different predictions. Possible values were usually suggested by careful study of the event. Tracks constructed by this method were generally better than those found graphically, because the individual hits on each track were selected by hand, instead of relying on software. Also, this method could predict coordinates in the slant chambers as easily as in the others, facilitating the use of the slants in determining a track. This was not the case in the graphical method where only the X and Y chambers were used to define a track, the slant hits being added at the end if they existed.

A final attempt at reconstructing non-hybridized tracks resembled the reconstruction by hand, as mentioned above, except a computer program, RECOVERY, was written to make the search. Using the vertex position and the λ and ϕ angles as starting points, a search for hits along the upstream road was made and the resulting track extrapolated to the mid-magnet plane. From there, successive lines were drawn to each hit in the EX chamber which was not part of a hybridized track. With the upstream and downstream track segments defined, an estimate of the momentum of the track was made as it was in FLOWERS. At this point SWIM was called and a search was made along the predicted downstream track segment for hits. This completed the construction of the track. The selection between multiple track solutions was done in the same manner as previously discussed.

Figures 13 through 15 show the momentum spectra for the tracks found by FLOWERS, by hand and with E743PIX, and those found by RECOVERY. The

similarity between these plots supports the conclusion that the recovery techniques did not bias our data.

Kinematics

The kinematics package was designed to attempt kinematic fits to the decay vertices, assigning a mass and a momentum to each decay track. The requirement that four-momentum be conserved at the secondary vertex provided four constraint equations:

$$\begin{aligned}
 C_1 &= \sum_{\alpha} p_{x\alpha} - p_x = 0 \\
 C_2 &= \sum_{\alpha} p_{y\alpha} - p_y = 0 \\
 C_3 &= \sum_{\alpha} p_{z\alpha} - p_z = 0 \\
 C_4 &= \sum_{\alpha} E_{\alpha} - E = 0,
 \end{aligned} \tag{10}$$

where the index α ranges over the decay products, and the variables without subscripts describe the decaying particle. Using the topology of the decay as a starting point, all kinematic hypotheses from a given list were tried. If all of the fit probabilities were low, an additional set of hypotheses containing neutral particles was tried.

A kinematic fit to an secondary event was accomplished by minimizing the χ^2 of the fit, subject to the constraints. In practice, this was done in the standard way by minimizing the function M , defined as:

$$M = \chi^2 + \sum_{\nu=1}^4 \lambda_{\nu} C_{\nu}, \tag{11}$$

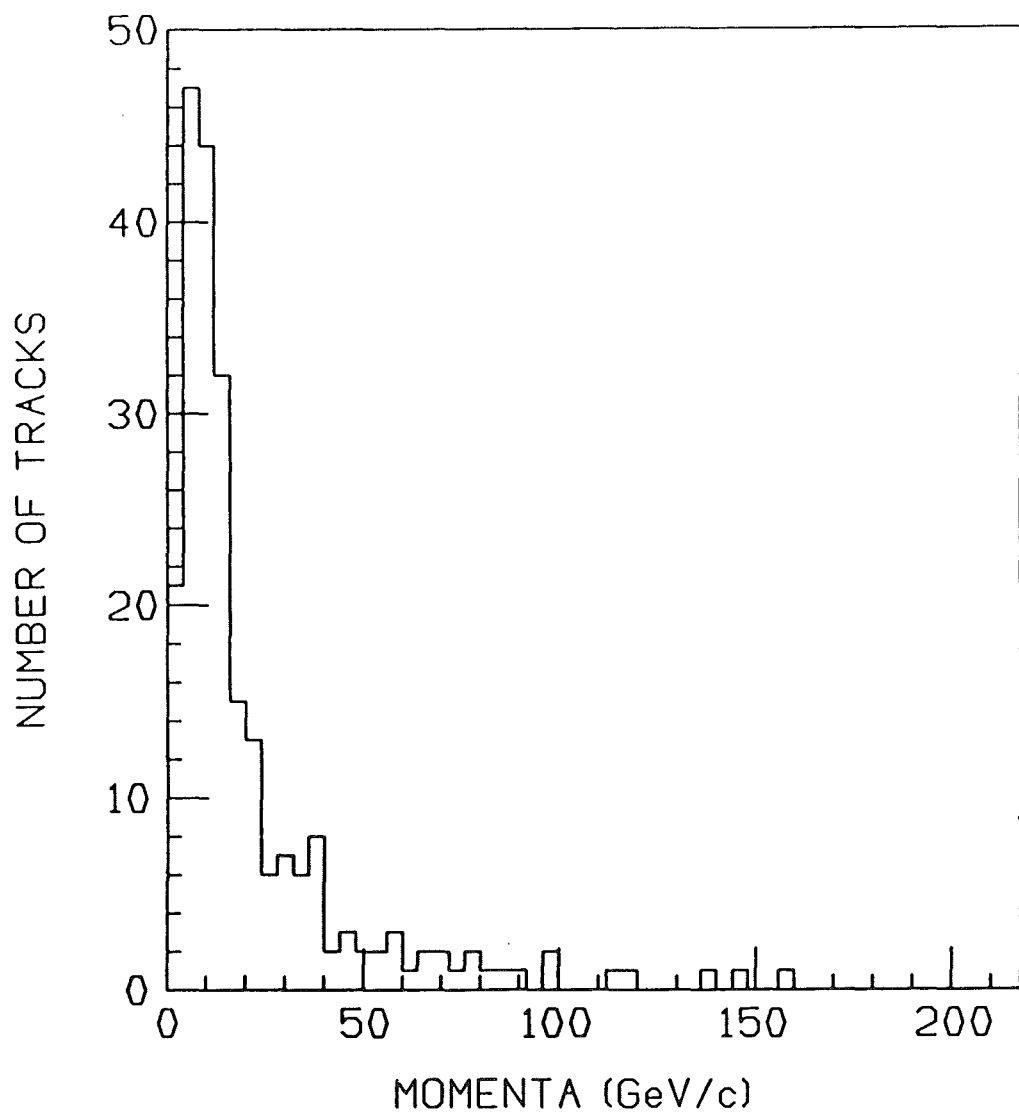


Figure 13. Momenta of tracks found by FLOWERS.

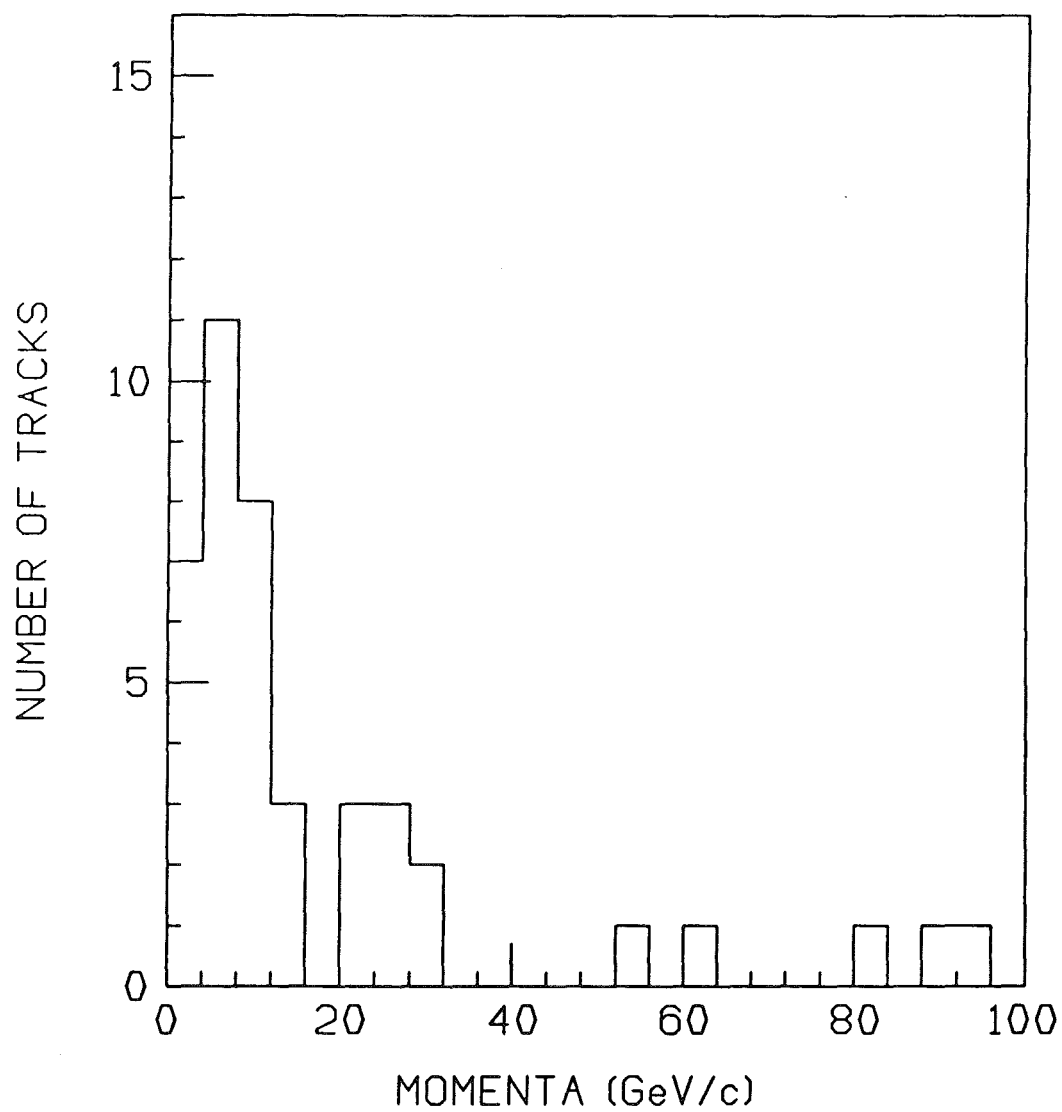


Figure 14. Momenta of tracks found by graphical techniques.

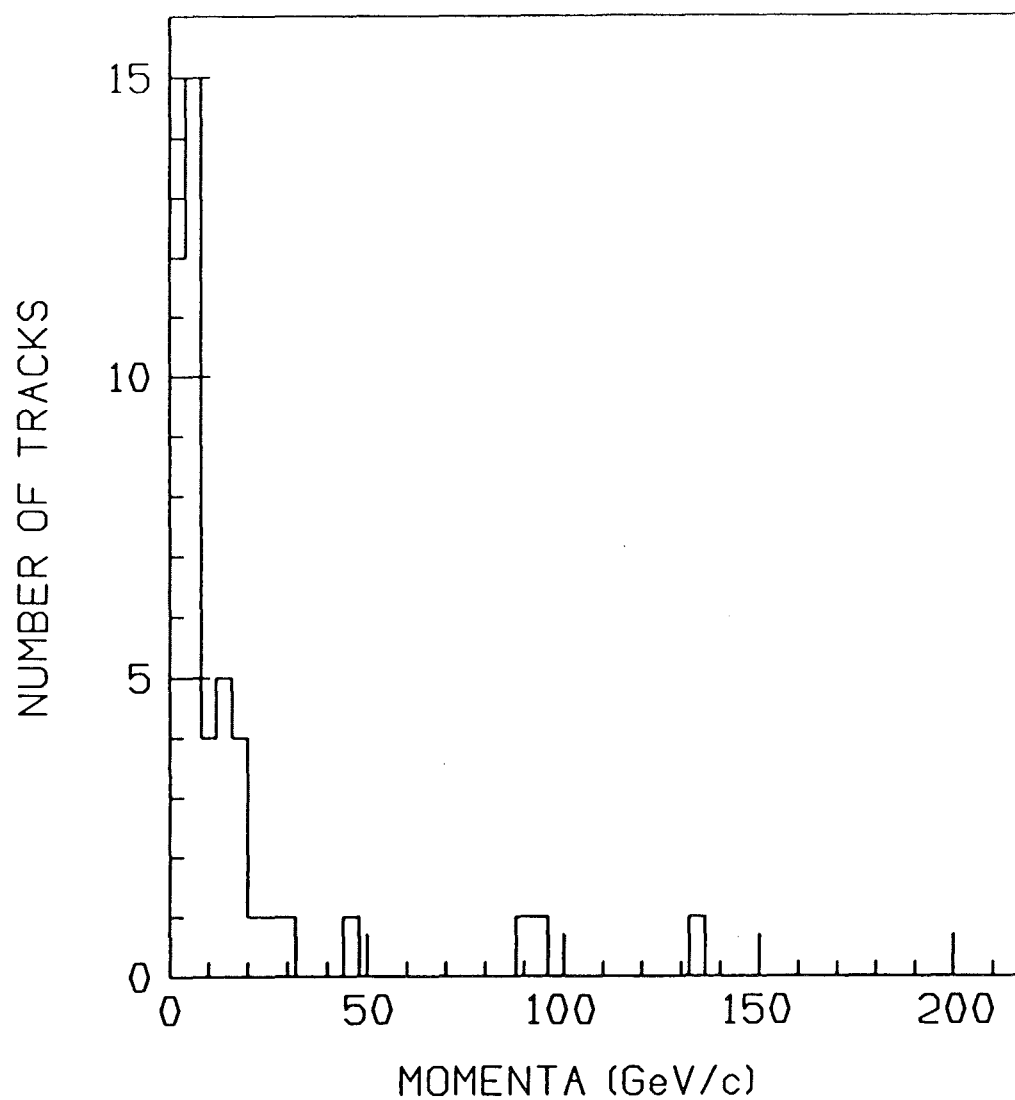


Figure 15. Momenta of tracks found by RECOVERY.

where the χ^2 is defined by:

$$\chi^2 = \sum_{i=1}^{3N} \sum_{j=1}^{3N} (p_i^{meas} - p_i^{fit}) \epsilon_{ij} (p_j^{meas} - p_j^{fit}). \quad (12)$$

In Equation (11), C_ν are the four constraint equations, and λ_ν are Lagrange multipliers. The summations from 1 to $3N$ in Equation (12) are over the three momentum components of the N decay particles. The measured momenta are those determined by GEOMETRY. The fitted momenta are adjusted to minimize the χ^2 . Incorporated into the inverse error matrix, ϵ , are the errors in the measured values of momentum, λ , and ϕ .

Constraint Classes

The determination of unknown momenta or energies required solving the constraint equations simultaneously, which was the objective of kinematic fitting. If all the quantities were known, the four constraints resulted in a trivial 4-C fit. In E743, we had no method of measuring the magnitude of the momentum of the decaying particle. In the best case, we could measure the vector-momenta of all secondary tracks, and the direction of the decaying particle. This would result in a 3-C fit. For each decay track for which we were unable to determine the magnitude of the momentum (i.e. a non-hybridized track), the constraint class of the fit was reduced by one, with a corresponding reduction in the quality of the fit. A special constraint class was the 0-C fit. This occurred when all of the decay tracks were hybridized, but the kinematics program found only low probability fits and therefore tried fits with missing neutral particles. Since we had no

neutral particle detection, we knew neither the magnitude of the momentum nor the angles of the neutral particle. This reduced what would have been a 3-C fit to a 0-C fit. Generally, there are two solutions to a 0-C fit, but one solution is sometimes unphysical.

Particle Identification

As described before, the three particle identification detectors in E743 were Č-short, Č-long, and the TRD. Particle identification played an important role in event analysis when it was used in conjunction with kinematics. Quite often there would be competing kinematic hypotheses, and particle identification could help discriminate between them. As an example, consider these four decay hypotheses:

$$D \rightarrow K\pi\pi$$

$$\rightarrow \pi K\pi$$

$$\Lambda_c \rightarrow pK\pi$$

$$\rightarrow Kp\pi.$$

All four hypotheses are possible results of kinematic fits to the same C3 decay vertex. Determining whether the decay particle is a D or a Λ_c reduces to the problem of whether there is a proton, p , in the decay products or not. Once that is determined, there are still two possible decays, resulting in different kinematic quantities for the decay particle.

Čerenkov Radiation Detectors

The Čerenkov detectors were basically the same, though they operated in different momentum ranges. The analysis programs were slightly different because the mirrors in Č-short were positioned very symmetrically. This symmetry was exploited when determining the fraction of light reflected from each mirror.

The identification procedure began with the determination of which mirrors reflected light from each track, and which mirrors were confused (i.e. contained light contributions from more than one track). Since the momentum of each track was known, the size of the light cone, hence the amount of light produced, was determined by the mass of the particle. Each mass hypothesis was tried, and the calculated light contributions were compared to the real light recorded in the cells. The correctness of each mass hypothesis was then calculated in the form of a probability. In order to maintain confidence in the results from Č-short and Č-long, verbose computer output was studied by hand on an event by event basis in order to understand the results in a way that would be impossible to program into a computer. In this way, decisions could be made by hand.

Transition Radiation Detector

As mentioned before, the TRD consisted of twenty PWCs, each preceded by a radiator panel filled with carbon fibers. As a charged particle passed through the radiators, transition radiation was created. This radiation entered the PWCs and, through photoabsorption, released electrons which were then detected at the

sense wires. The spectrum for this deposited energy follows a Landau distribution. By the Central Limit Theorem, the distribution of the averages of multiple samplings of almost any finite distribution will approach a Gaussian distribution. The Landau distribution has an infinite tail, but due to kinematic restrictions on the maximum energy which can be transferred to an electron, our distribution was truncated, forcing it to be finite. As a track passed through the TRD, the energy deposited in the planes was averaged. There was a requirement that at least twelve planes contribute in order to approximate the Gaussian energy distribution.

In order for a plane to contribute to the average energy deposited from a track, it was required that it contain a clean hit which corresponded to the track. A clean hit meant that only one track from FLOWERS struck this wire, and that the adjacent wires in the plane were not struck. Taken together, these conditions insured that the energy deposited on a given wire was a result of the passage of the track in question.

Once it was determined that a track produced enough clean hits in the TRD, the energies deposited were averaged. For each mass hypothesis, using the measured momentum, γ (Lorentz) was calculated. A look at the experimentally determined reference distribution, Figure 16, gave the expected energy deposited for the calculated γ . Using the Gaussian distribution and the difference between the expected and observed energies, a probability was calculated.

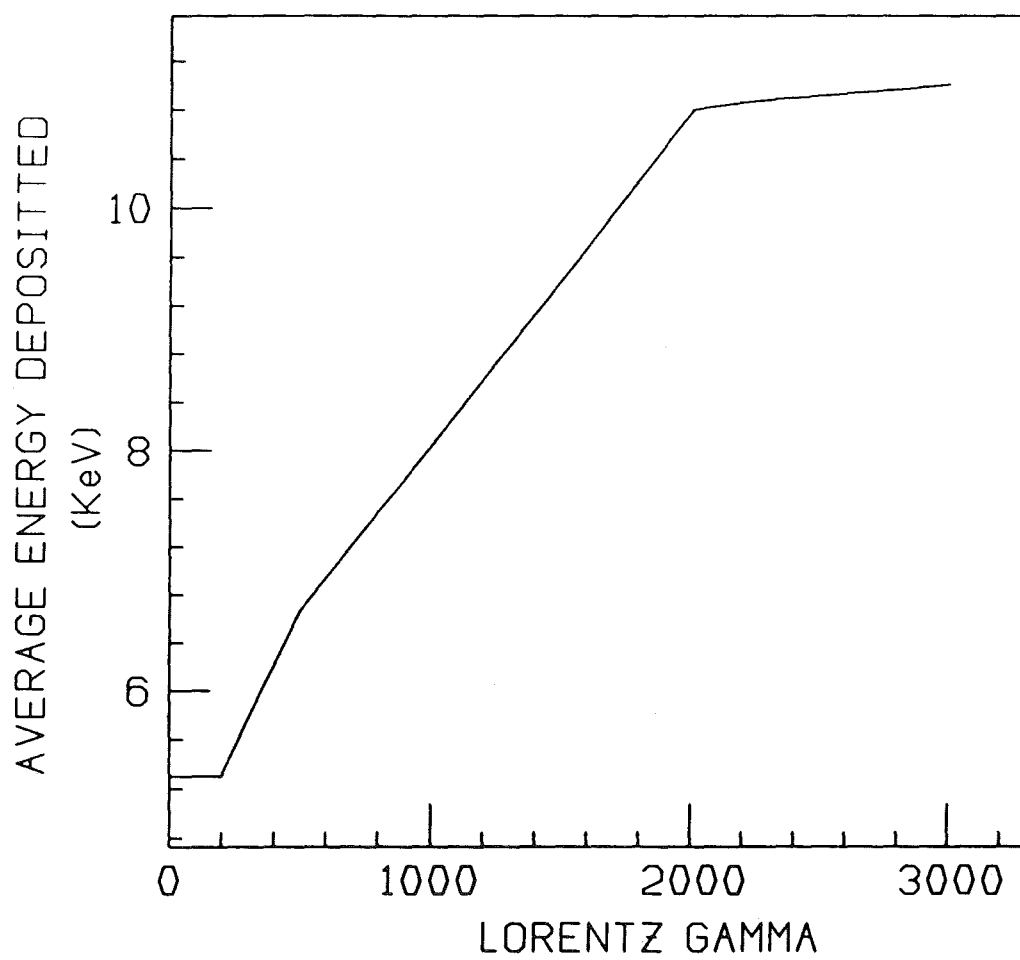


Figure 16. TRD reference distribution used in particle identification.

CHAPTER V

CHARM HADROPRODUCTION RESULTS

Total D/\bar{D} Cross Sections

Our total data sample consisted of approximately 1.2×10^6 triggered events. The calculation of the total cross section was restricted to events with C3/X3 and V4/X4 topologies. This was done to eliminate much of the strange background associated with V2 or C1 topologies. The total D/\bar{D} cross section was computed using the following formula:

$$\sigma(D/\bar{D}) = \frac{N_{\text{obs}}(D/\bar{D}) \cdot W_{\text{MC}}}{S \cdot \epsilon_s \cdot BR} \quad (13)$$

In equation (13), N_{obs} is the number of observed decays which decay via the mode with branching ratio BR . In E743, the modes we considered were topological ones. We were then able to use well known topological branching ratios, rather than the poorly known exclusive branching ratios.[57] W_{MC} is the Monte Carlo calculated visibility weight which corrects for data cuts and scanning losses. S is the experimental sensitivity (events/ μb), and ϵ_s is the double scan efficiency (0.95 ± 0.05).

The sensitivity S is a the result of a calculation made to determine the total number of interactions expected given the target and beam parameters. It is

calculated using the formula:

$$S = \frac{L_H \cdot \rho_H \cdot N_A \cdot N_B}{A_H} \left(\frac{\text{events}}{\mu\text{b}} \right) \quad (14)$$

In equation (14), L_H is the length of the fiducial volume of LEBC, ρ_H is the density of the hydrogen in LEBC, N_A is Avogadro's number, N_B is the number of usable beam tracks on the scanned film, and A_H is the atomic number of hydrogen. For our experiment, $S = 11.8 \pm 0.6(\text{events}/\mu\text{b})$.

Visibility Cuts and Weights

Visibility cuts were applied to our charm sample to reduce background from strange particle, Λ_c , and D_s decays. They were also used to insure high detection efficiency. The charm box cut mentioned before was applied during the scanning and measuring stages. The five additional topological cuts are listed below.

1. The decay length was required to be ≥ 1 mm. This insured that the decay was visible on the scanning table. It also suppressed the decays from the Λ_c and the D_s , whose lifetimes are shorter than that of the D .
2. All impact parameters were required to be $\geq 20 \mu\text{m}$ in at least one of the views. This cut once again suppressed Λ_c and D_s decays, but more importantly it removed V2 decays which were superimposed on other tracks and mistakingly labelled as C3 decays.
3. The maximum impact parameter was required to be $\geq 50(100) \mu\text{m}$ and $\leq 1000(2000) \mu\text{m}$ for neutral(charged) D s. These cuts once again reduce

the contamination by Λ_c and D_s decays which tend to have small opening angles, and from misidentified interactions, which tend to have large impact parameters.

4. The opening space angle between any two decay tracks was required to be ≥ 2 mrad in at least one view. This cut was applied in order to suppress the Σ^+ Dalitz decay ($\Sigma^+ \rightarrow p\pi^0 \rightarrow pe^+e^-$). These decays would appear and be identified as C3 decays.
5. Lastly, to insure good spectrometer acceptance and help remove interactions, the track angles λ and ϕ were required to be ≤ 150 mrad for $(n-1)$ of the decay tracks.

Table 12 lists the results of the visibility cuts. The numbers listed after each category are the number of events removed due to the particular cut. The topological branching ratios and visibility weights are also given.

To correct for D decays which would be discarded due to the application of the visibility and topology cuts, or occur beyond the LEBC volume, it was necessary to weight each topology with a visibility weight. This weighting was accomplished by multiplying each event by the reciprocal of its detection probability. The detection probability was calculated by studying Monte Carlo generated events of the form $pp \rightarrow D\bar{D}X$ assuming the standard $(1 - |x_F|)^n e^{-bp_\perp^2}$ spectrum, and using the world averages of 0.43 ps (D^0/\bar{D}^0) and 0.92 ps (D^\pm) for the mean lifetimes of the mesons. The values for n and b used were determined from our own data.

TABLE 12
 D/\bar{D} CROSS SECTION DATA SAMPLE

	C3/X3	V4/X4
Total Number of Decays	94	23
Decay Length Cut	13	4
Track Angle Cuts	9	1
Min. Impact Parameter Cut	11	2
Max. Impact Parameter Cut	13	3
Total After Cuts	48	13
Branching Ratios	0.43 ± 0.10	0.17 ± 0.04
Visibility Weights	2.1 ± 0.2	3.2 ± 0.4

The visibility weights listed in Table 12 varied less than 7% with a 25% change in n , and less than 1% with a 25% change in b .

Results

Inserting the above results into Equation (13) yields D/\bar{D} cross sections for all $x_F[58]$ of:

$$\sigma(D^+/D^-) = (20.9 \pm 6.9)\mu\text{b}$$

$$\sigma(D^0/\bar{D}^0) = (21.8 \pm 3.6)\mu\text{b}$$

$$\sigma(D/\bar{D}) = (42.7 \pm 7.8)\mu\text{b}.$$

The errors quoted above are statistical. The most dominant systematic error is a 25% uncertainty in the branching ratios. All other systematic errors are at or below the 5% level.

Differential D/\bar{D} Cross Sections

The study of differential cross sections gives clues to the internal structure of hadrons and the mechanisms by which they interact and are produced. It also provides tests for the predictions of QCD production models.

Selection Criteria and Weights

All decays which took place inside the charm box were examined for possible inclusion into the fitted sample. As with the total cross section sample, visibility cuts were first applied. Decays in which all impact parameters were $\leq 10 \mu\text{m}$ were considered to be ionization jumps and were rejected. Any charged (neutral) decay having an impact parameter ≥ 2000 (1000) μm was considered an interaction and rejected.

Kinematic cuts were then applied. All 1C fits were considered to be unreliable and discarded. To suppress strange particle background, any C1 or V2 was required to have a track with $p_{\perp} \geq 250 \text{ Mev}/c$. All C3 decays were examined for a track with a non-zero impact parameter. Once found, if the remaining tracks gave a kinematic fit to a γ , K^0 , Λ^0 , or D^0 , then the topology was changed to a V2. The V2 and C1 topologies were only accepted if there was also a C3, V4, or C5 decay in the same event.

The kinematic results for the remaining events were scrutinized in order to determine which had acceptable D/\bar{D} fits. Any 3C fit was required to have a fit probability $> 0.1\%$, while a 2C fit was required to have a fit probability $> 1.0\%$. Any 0C fit with two solutions for which $\Delta x_F > 0.1$ was rejected. Any 0C fit for which there were acceptable fits to D , D_s , and Λ_c was rejected as ambiguous. Any fit which calculated the lifetime > 10 times the world average was rejected.

The selection of the correct fit, when more than one was offered by the kinematics program, followed a defined hierarchy. 3C fits were accepted before 0C fits. Cabibbo favored fits were accepted over Cabibbo suppressed fits. Hadronic fits were favored over semi-leptonic fits. Particle identification information was used whenever possible to veto kinematic hypothesis, or to uniquely identify an electron in a semi-leptonic decay. Since the spectrometer acceptance was well known for events with $x_F \geq 0.0$, the fitted sample was restricted to this range and contained 15 events.

The total weight for a fit was a product of the visibility weight and the spectrometer weight. The visibility weight was given by:

$$W_{vis} = \frac{1}{e^{-t_{min}/\tau} - e^{-t_{max}/\tau}} \quad (15)$$

where τ is the world average of the D lifetime, and t_{max} and t_{min} are the limiting decay times for which the decay will pass all visibility cuts. The spectrometer weights were found by Monte Carlo simulation of events and applying cuts which

corresponded to spectrometer acceptance. Included in this weight was an estimate of the hybridization efficiency.

Results

The values of n and b in the parameterization:

$$\frac{d^2\sigma}{dx_F dp_\perp^2} \sim (1 - |x_F|)^n e^{-bp_\perp^2} \quad (16)$$

were found by calculating a maximum likelihood fit to Equation (16). The results of this fit are:

$$\begin{aligned} n &= 8.4_{-1.9}^{+2.2} & \langle x_F \rangle &= \frac{1}{n+2} = 0.10 \pm 0.02 \\ b &= 0.78_{-0.16}^{+0.19} (\text{GeV}/c)^{-2} & \langle p_\perp^2 \rangle &= b^{-1} = 1.3 \pm 0.3 (\text{GeV}/c)^2. \end{aligned}$$

Figures 17 and 18 are the $d\sigma/dx_F$ and $d\sigma/dp_\perp^2$ distributions, respectively. The solid lines correspond to the parameterizations as characterized by the fitted values stated above.

D^*/\bar{D}^* Meson Production

Only one decay channel for D^* mesons could be detected by us, namely $D^{*+} \rightarrow D^0\pi^+$, and its charge conjugate. This restriction was due to the lack of neutral particle and gamma detectors in our spectrometer.

The selection of D^* candidate events was restricted to those V4 and X4 events which passed the cuts for the topological cross section calculations. Further, it was required that there be a 0C, 2C, or 3C kinematic fit to a D^0 which was

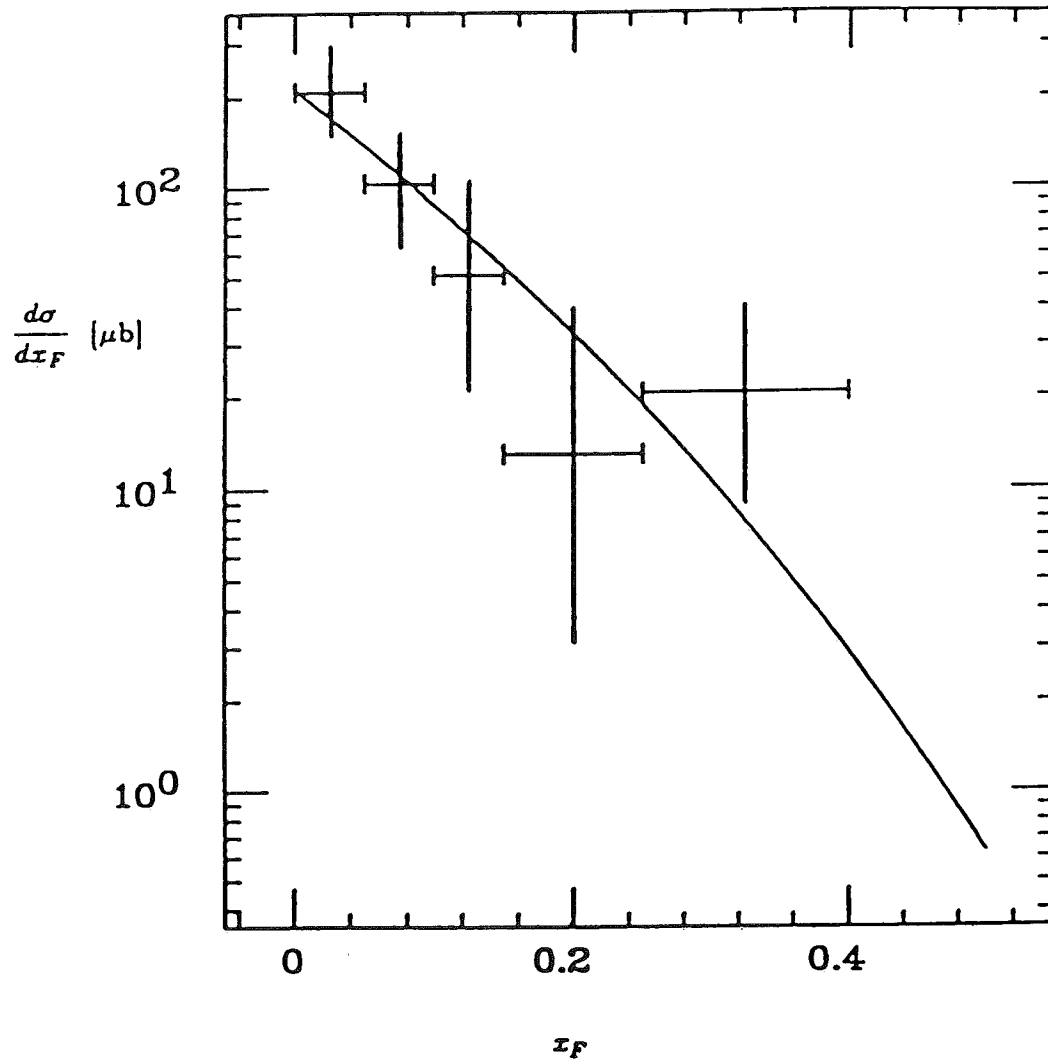


Figure 17. The $d\sigma/dx_F$ distribution for D/\bar{D} mesons.

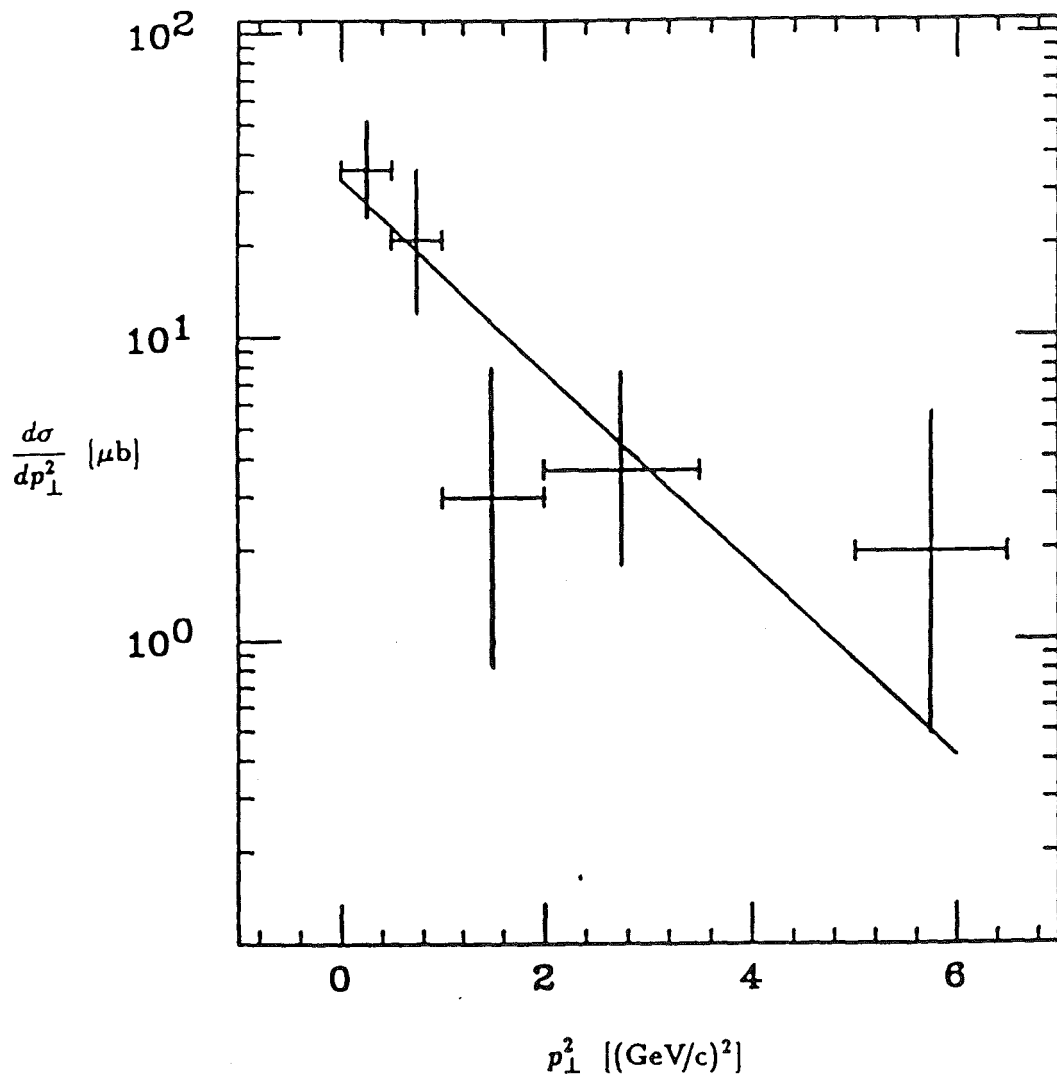


Figure 18. The $d\sigma/dp_{\perp}^2$ distribution for D/\bar{D} mesons.

consistent with particle identification results. The same hierarchy used for the differential cross section sample was employed to choose between competing kinematic fits. From a total of twenty-four V4/X4 events, eleven passed the above mentioned criteria. This data sample consisted of three unambiguous D^0 decays, six unambiguous \bar{D}^0 decays, and two D^0/\bar{D}^0 ambiguous decays.

Analysis

Since the D^* decays strongly, the decay vertex is too close to the production vertex to be resolved in LEBC. The mass difference between the $D^{*\pm}$ and the $D^0\pi^+$ systems is $5.90 \pm .09$ MeV/ c^2 . This is known as the Q-value of the decay, and is the total amount of kinetic energy available to the decay particles. With such a low Q-value for this decay, the opening angle, in the laboratory, between the D^0 and π^+ is necessarily small.

To determine which D^0 s came from $D^{*\pm}$ decays, the invariant mass of the kinematically fitted D^0 and a pion from the primary vertex was calculated. The only primary tracks considered were those hybridized in GEOMETRY, since the vector momentum was needed. When the decay was unambiguously a $D^0(\bar{D}^0)$, only combinations using a $\pi^+(\pi^-)$ were made. Otherwise, combinations using both charged pions were made. Exploiting the low Q-value of the D^* decay, only the invariant mass corresponding to the smallest opening decay angle was plotted.

The background was determined by producing similar invariant mass combinations from each D^0 and the primary pions from all of the other events. The area of this histogram was then normalized to the area of our original invariant mass

plot. The invariant mass plot with the background superimposed can be seen in Figure 19.

The pion from a D^* decay has a low momentum and may not be in the acceptance of the spectrometer. To correct for this, each reconstructed D^* was assigned a weight determined by Monte Carlo simulation. At the D^* vertex position, D^* s were generated using the x_F and p_\perp distributions determined from our sample of D s. This is a good approximation since the proton beam was unpolarized, the mass difference between the D and D^* is small, and both types of mesons have the same isospin. The decay of the D^* was then generated with the correct pion charge, and the pion was swum through the magnetic field. If the pion was within the acceptance of every wire chamber up to and including EX, it was considered to be reconstructed. These Monte Carlo events were histogrammed as a function of the x_F of the D^* . The weight for the real D^* event was then calculated as the inverse of the reconstruction probability, at the x_F under consideration. The weighted invariant mass plot can be seen in Figure 20, and was used for the subsequent analysis. The characteristics of the three D^* events are displayed in Table 13.

Results

As can be seen from Figure 20, the weighted D^* peak represents 4.15 events, with a background of 0.23 events. The total number of decays from the channel $D^{*\pm} \rightarrow D^0 \pi^\pm$ is then 3.92.

TABLE 13
 D^* DATA SAMPLE

Roll	Frame	ID	p_{\perp}	x_F	Weight
1012	2224	D^{*+}	1.85	-.0135	1.54
1014	1863	D^{*-}	1.47	.2893	1.00
1088	1340	D^{*+}	1.25	-.0567	1.61

Assuming a binomial distribution, the expected value is:

$$np \pm \sqrt{n(p)(1-p)} = 2.97 \pm 1.47, \quad (17)$$

where $n = 11$ is the number of sampled events and $p = .27$ is the theoretical probability explained in Chapter II.

Using the error found from the binomial distribution as the statistical error on the number of $D^{*\pm}$ s seen, we can calculate the cross section for $D^{*\pm}$ production as follows:

$$\begin{aligned} \sigma(D^{*\pm}) &= \frac{\sigma(D^{*\pm} \rightarrow D^0 \pi^{\pm})}{\sigma(D^0)} \cdot \frac{\sigma(D^0)}{\text{BR}} \\ &= 13.31 \pm 5.74 \mu\text{b}. \end{aligned} \quad (18)$$

In Equation (18), BR is the branching ratio for the decay observed, and $\sigma(D^0)$ is the topological cross section determined previously.

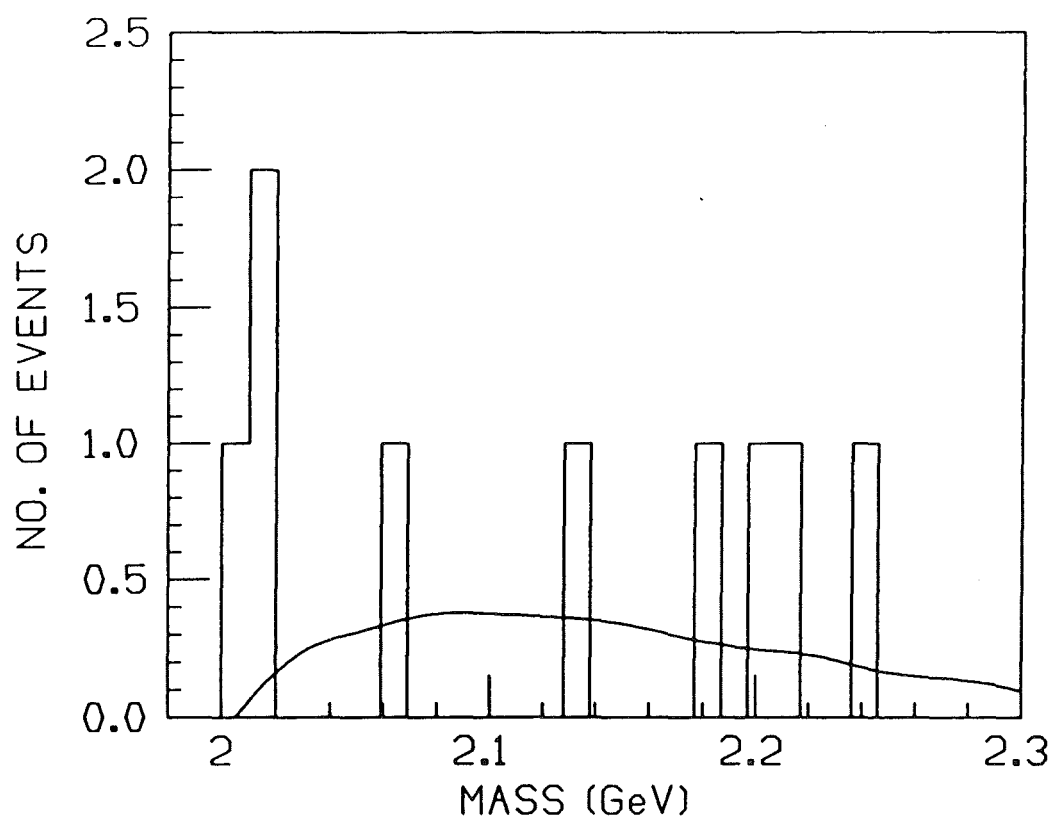


Figure 19. Invariant mass plot showing the D^* mass peak and the superimposed background curve.

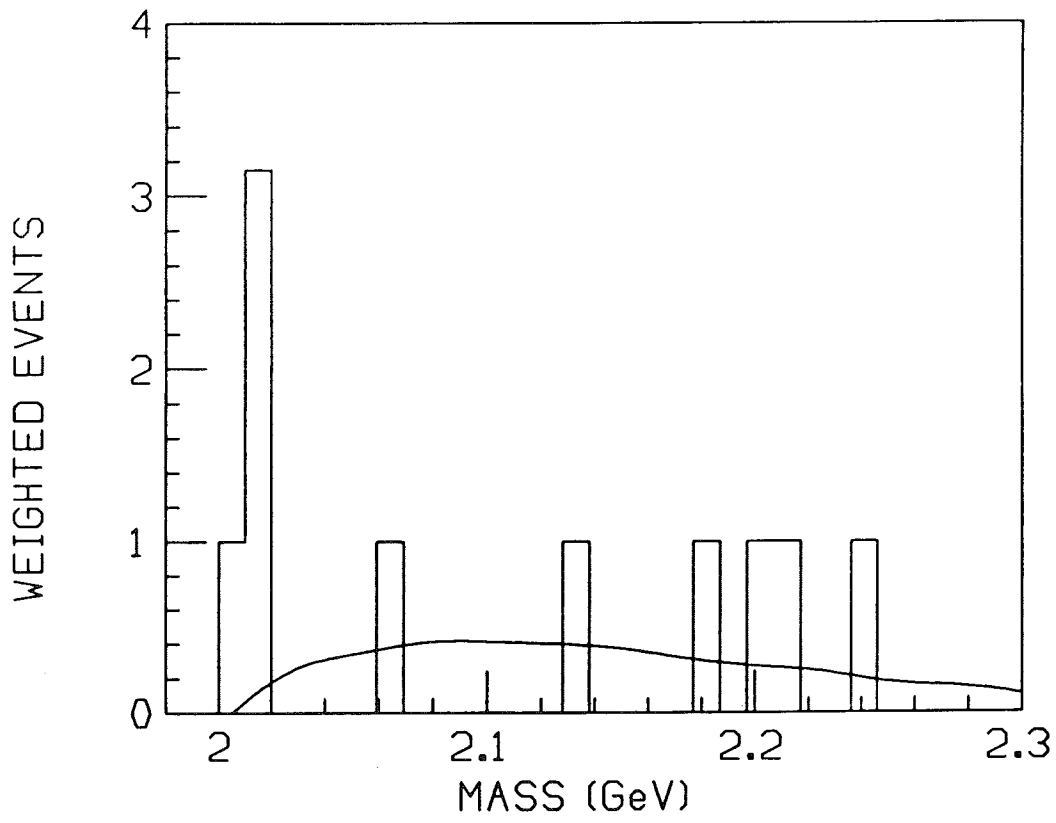


Figure 20. Weighted invariant mass plot showing the D^* mass peak and the superimposed background curve.

CHAPTER VI

CONCLUSIONS

D/\bar{D} Total Cross Section

As mentioned in Chapter II, the total inclusive cross section calculated using perturbative QCD is highly dependent on the choice of input parameters. A more sensitive test of QCD involves taking the ratio of cross sections at different energies. Table 14 shows the theoretical results of these QCD calculations, using the lowest order terms in the perturbative expansion, at E743 and NA27 energies.

TABLE 14
ENERGY DEPENDENCE OF $\sigma(D/\bar{D})$

Structure Function	$\frac{\sigma(D/\bar{D}) (\sqrt{s}=38.8 \text{ GeV})}{\sigma(D/\bar{D}) (\sqrt{s}=27.4 \text{ GeV})}$			
$m_c \text{ (GeV/c}^2\text{)}$	1.20	1.25	1.30	1.40
DO-1	1.70	1.80	1.85	1.95
EHLQ-1	1.85	1.90	1.95	2.10

The calculations in Table 14 were performed using the parameterization of the strong coupling constant:

$$\alpha_s(\mu^2) = \frac{12\pi}{25\ln(\mu^2/\Lambda^2)}, \quad (19)$$

with $\Lambda = 0.2$ GeV, $\mu = 2m_c$, and contributions from four quark flavors..[59]

The cross sections from E743 and NA27 give the result:

$$\frac{\sigma(D/\bar{D}) (\sqrt{s} = 38.8 \text{ GeV})}{\sigma(D/\bar{D}) (\sqrt{s} = 27.4 \text{ GeV})} = \frac{42.7 \pm 6.8 \mu\text{b}}{30.2 \pm 3.3 \mu\text{b}} = 1.4 \pm 0.3, \quad (20)$$

which falls within the theoretical range if $m_c = 1.2 - 1.4$ GeV/c². The theoretical uncertainties in μ can also be taken into account. In Figure 21, the total inclusive D/\bar{D} cross section from E743, normalized to the value at $\sqrt{s} = 27.4$ GeV from NA27, is shown. The hatched band represents the range of Fusion Model predictions as μ^2 is varied from $4m_c^2$ to \hat{s} , and m_c is varied between 1.2 and 1.4 GeV/c². The DO-1 and EHLQ-1 structure functions were both used in the Fusion Model calculations, and Λ was taken to be 0.2 GeV. The total inclusive cross section from E743 is superimposed on the plot, and is consistent with the theoretical results. This result supports the use of QCD and the Fusion Model in the description of heavy flavor hadroproduction.

D/\bar{D} Differential Cross Sections

The predictions of the Fusion Model indicate central production, with a rising peak in the differential cross section for heavy quark hadroproduction at $x_F = 0$

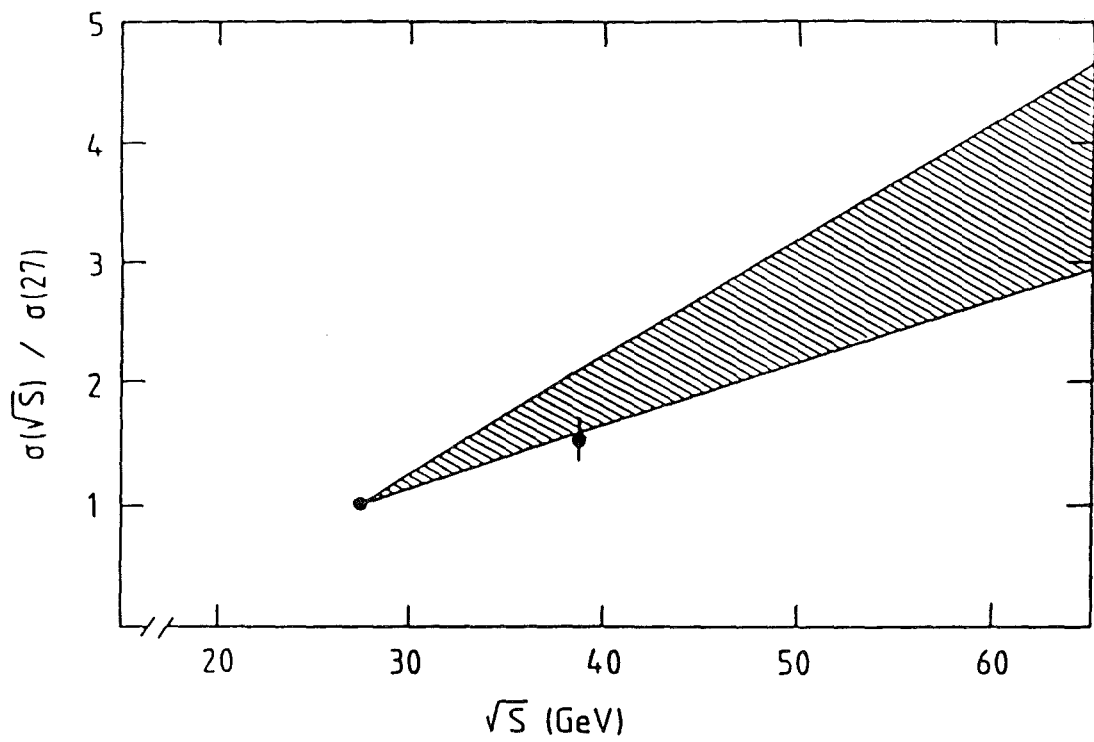


Figure 21. Energy dependence of the inclusive D/\bar{D} total cross section, normalized to $\sigma(D/\bar{D})$ at $\sqrt{s} = 27.4$ GeV.

as \sqrt{s} increases. This effect is seen in the comparison of results from E743 and NA27. As \sqrt{s} increased from 27.4 GeV to 38.8 GeV, n increased from 4.9 ± 0.5 to $8.4^{+2.2}_{-1.9}$, and $\langle x_F \rangle$ decreased from 0.15 ± 0.02 to 0.10 ± 0.02 . Figure 22 shows the fit to our data with the predictions of the Fusion Model superimposed. The Lund hadronization method and the basic parton model were both used. The EHLQ-1 structure functions were used with a quark mass $m_c = 1.25 \text{ GeV}/c^2$. [60]

The Fusion Model also predicts that the average transverse momentum of the charm quark should be on the order of its mass. Figure 23 shows the fit to our data with the Fusion Model results superimposed. Once again, the results using both the basic parton model and the Lund hadronization techniques are displayed, with the same conditions stated above. The value of $\langle p_\perp \rangle = 1.1^{+0.2}_{-0.1} \text{ GeV}/c$ obtained from E743 is consistent with a quark mass of $m_c = 1.25 \text{ GeV}/c^2$.

D^*/\bar{D}^* Summary

The prediction of 2.97 ± 1.47 events from the decay of $D^{*\pm}$ into $D^0\pi^\pm$ was obtained using a binomial distribution and the following assumptions concerning D^* and D production:

1. D mesons are only produced directly or through the decay of a D^* meson.
2. Direct production of D mesons occurs at the same rate as direct production of \bar{D} mesons.
3. Direct production of D^0/\bar{D}^0 mesons occurs at the same rate as direct production of D^\pm mesons. The only asymmetry in the total production rates is

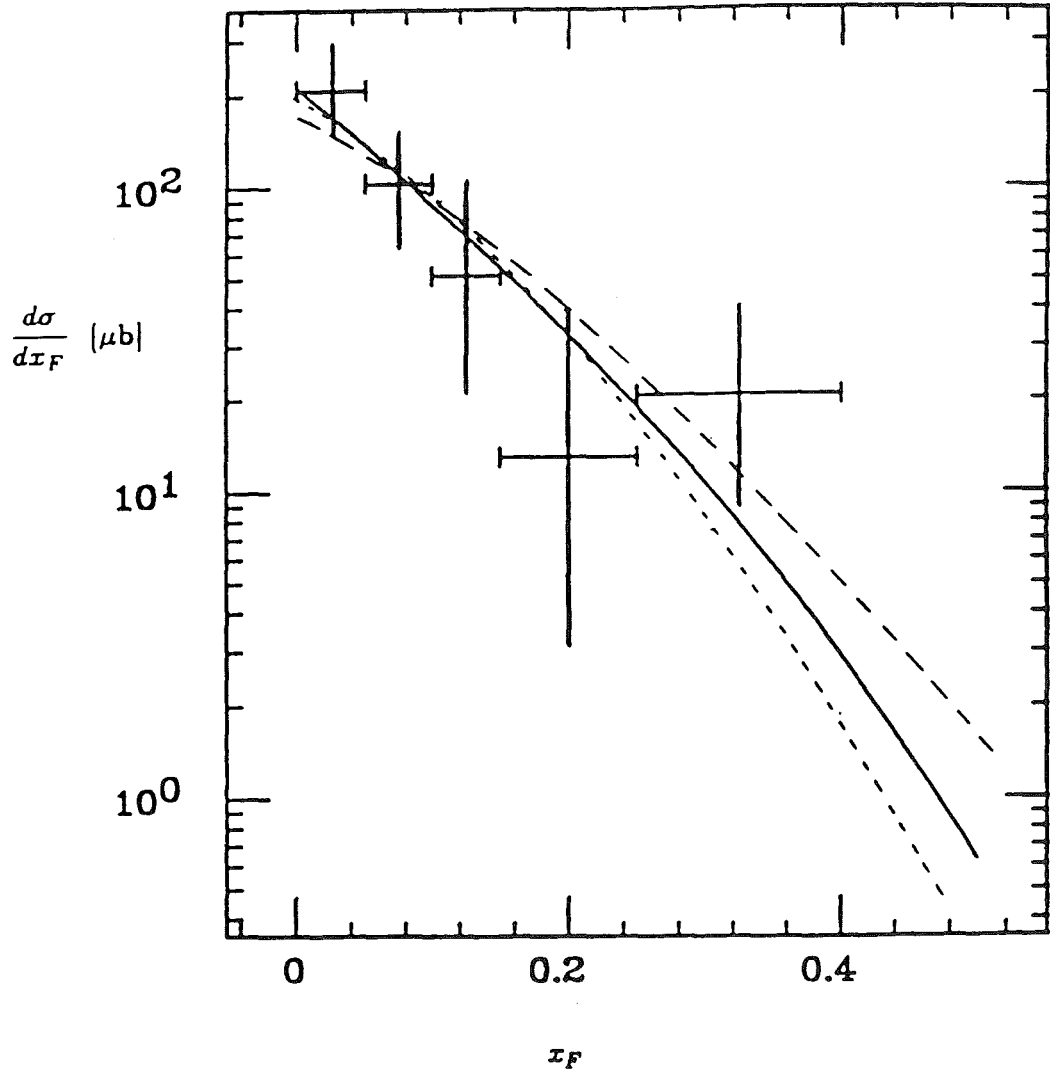


Figure 22. Comparisons of Fusion Model predictions to the measured $d\sigma/dx_F$ distribution. The solid curve shows the fit to $d\sigma/dx_F \propto (1 - |x_F|)^n$ with $n = 8.4$. The dotted curve represents predictions of the Fusion Model using the basic parton hadronization, while the dashed curve uses the Lund hadronization techniques.

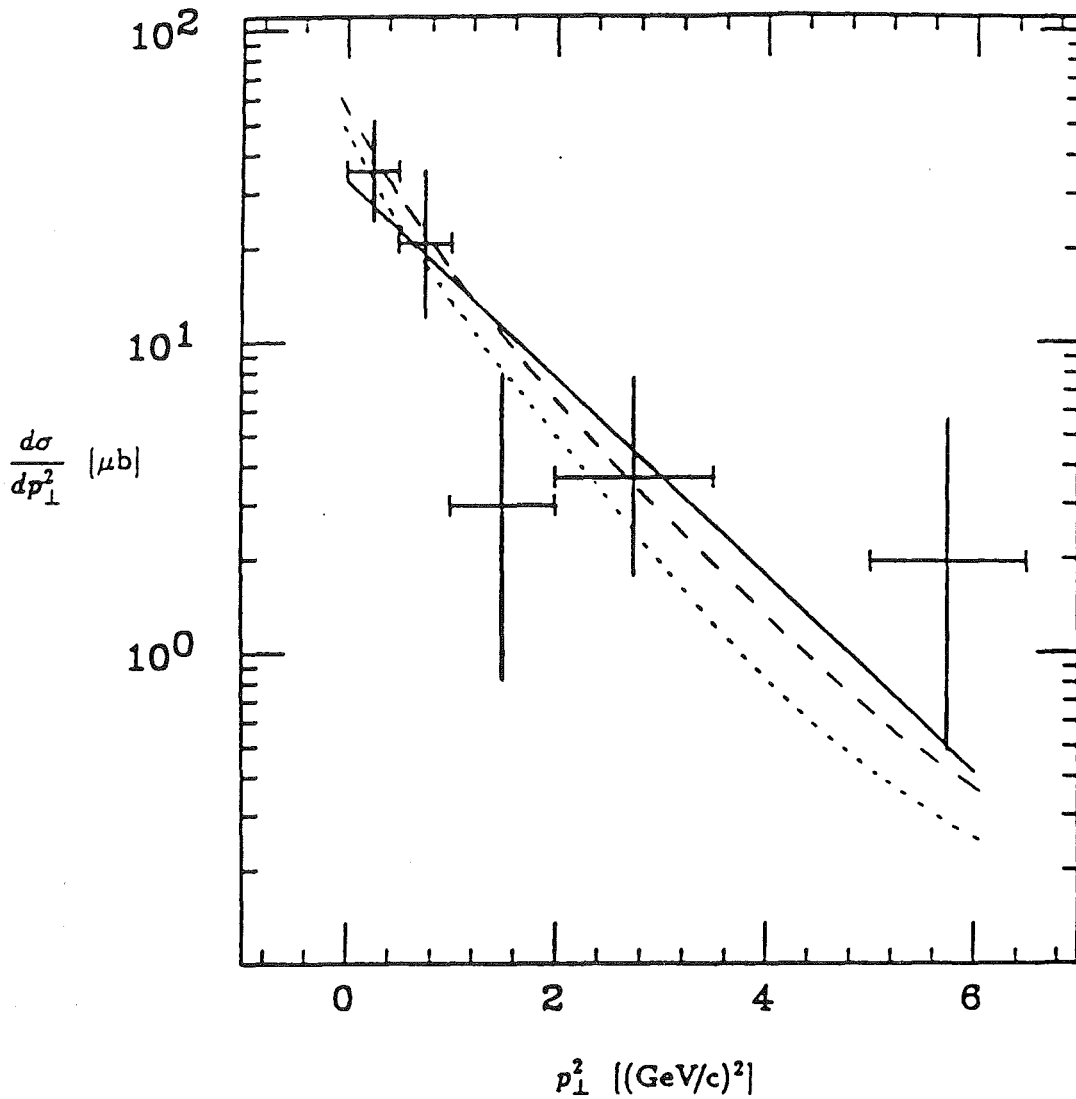


Figure 23. Comparisons of the Fusion Model predictions to the measured $d\sigma/dp_{\perp}^2$ distribution. The solid curve shows the fit to $d\sigma/dp_{\perp}^2 \propto e^{-bp_{\perp}^2}$ with $b = 0.8$. The dotted curve represents predictions of the Fusion Model using the basic parton hadronization, while the dashed curve uses the Lund hadronization techniques.

attributed to the production of D^* mesons, which decay preferentially into D^0/\bar{D}^0 mesons.

4. The D^* mesons are produced at three times the rate of D mesons. Since the D^* mesons have total angular momentum $J=1$, there are three angular momentum states available for each state available to the D^0 mesons, which have total angular momentum $J=0$.

Despite the low statistics in this analysis, the measured number of events from the $D^{*\pm} \rightarrow D^0\pi^\pm$ decay, 3.92, is in agreement with the predicted value of 2.97 ± 1.47 . This result supports the model assumptions stated above. The total production cross section for $D^{*\pm}$ is then calculated to be $\sigma(D^{*\pm}) = 13.31 \pm 5.74 \mu\text{b}$.

APPENDIX

The primary purpose of E743 was to measure the total charm hadroproduction cross section in proton-proton collisions at a beam momentum of 800 GeV/c. This represented the highest fixed target beam momentum for an experiment of this kind. E743 was proposed as a follow up to NA27, which used the same bubble chamber, LEBC, and the same trigger configuration at a beam momentum of 400 GeV/c. The data taking run for E743 spanned the time period from May, 1985, through August, 1985.

The following is a list of collaborators from E743:

III. Physikalisches Institut der Technischen Hochschule, Aachen
V. Commichau, A. Roth, W. Struczinski, P. Bosetti

Institut für Hochenergiephysik der AdW, Berlin/Zeuthen
U. Gensch, D. Knauss, T. Naumann, H. Nowak

Tata Institute of Fundamental Research, Bombay
S. Banerjee, S. N. Ganguli, A. Gurtu,
P. K. Malhotra, R. Raghavan, A. Subramanian

Inter-University Institute for High Energies, Brussels
J. Lemonne, B. Vonck

CERN, European Organization for Nuclear Research, Geneva
J. J. Hernandez, J. Hrubec, M. Iori, H. Leutz, A. Poppleton, M. C. Touboul

Duke University, Durham
P. C. Bhat, A. T. Goshaw, G. E. Mendez, W. J. Robertson

Fermilab, Batavia
R. L. Dixon, H. C. Fenker, L. Voyvodic

Northeastern University, Boston
I. Leedom, S. Reucroft, C. Zabounidis

University of Kansas, Lawrence
R. Ammar, J. Gress, X. Liu

University of Michigan, Ann Arbor
R. C. Ball, T. Coffin, T. Dershem, L. W. Jones, B. P. Roe, M. Weber

Michigan State University, East Lansing
C. Bromberg, A. Nguyen

Université del l'Etat à Mons, Mons
J. F. Baland, V. P. Henri, P. Legros, P. Pilette

University of Notre Dame, South Bend
R. Brun, G. E. Canough, N. Giokaris, S. Mikocki, J. Poirier

Vanderbilt University, Nashville
J. M. Marraffino, C. E. Roos, M. Senko, J. W. Waters, M. S. Webster

University of Innsbruck, Innsbruck
P. Girtler, D. Kuhn, G. Neuhofer, K. Rasner

REFERENCES

1. C. Yang, and R. Mills, Phys. Rev. 96 (1954) 191.
2. T. Lee, and C. Yang, Phys. Rev. 104 (1956) 254.
3. R. Feynman, Phys. Rev. 76 (1949) 769.
4. S. Glashow, Nucl. Phys. 22 (1961) 579.
5. S. Weinberg, Phys. Rev. Lett. 19 (1967) 1264.
6. A. Salam, Elementary Particle Physics: Relativistic Groups and Analicity (Nobel Symposium # 8), ed. N. Svartholm (Almqvist and Wiksell, Stockholm, 1968) 367.
7. F. Halzen and A. Martin, Quarks and Leptons, John Wiley and Sons, Inc. (1984) 320.
8. G. Arnison *et al*, Phys. Lett. B 122 (1983) 103.
9. G. Arnison *et al*, Phys. Lett. B 126 (1983) 398.
10. R. Feynman, and M. Gell-Mann, Phys. Rev. 109 (1958) 193.
11. N. Cabbibo, Phys. Rev. Lett. 10 (1963) 531.
12. S. Glashow, J. Iliopoulos, L. Maiani, Phys. Rev. D 2 (1970) 1285.
13. A. Litke, *et al*, Phys. Rev. Lett. 30 (1973) 1189.
14. G. Tarnopolsky, Phys. Rev. Lett. 32 (1974) 432.
15. J. Aubert, *et al*, Phys. Rev. Lett. 33 (1974) 1404.
16. J. Augustine, *et al*, Phys. Rev. Lett. 33 (1974) 1406.
17. G. Goldhaber, *et al*, Phys. Rev. Lett. 37 (1976) 255.

18. I. Peruzzi, *et al*, Phys. Rev. Lett. 37 (1976) 569.
19. S. Tavernier, Rep. Prog. Phys. 50 (1987) 1439. HOBC results are from reference 21.
20. J. Ritchie, *et al*, Phys. Lett. B 126 (1983) 499.
21. H. Cobbaert, *et al*, Z. Phys. C 36 (1987) 577.
22. P. Fritze, *et al*, Phys. Lett. B 96 (1980) 427.
23. R. Ball, *et al*, Phys. Rev. Lett. 51 (1983) 743.
24. M. Duffy, *et al*, Phys. Rev. Lett. 55 (1985) 1816.
25. M. Duffy, *et al*, Phys. Rev. Lett. 57 (1986) 1522.
26. M. Jonker, *et al*, Phys. Lett. B 96 (1980) 435.
27. M. Aguilar-Benitez, *et al*, Phys. Lett. B 135 (1984) 237.
28. M. Aguilar-Benitez, *et al*, Phys. Lett. B 189 (1987) 476.
29. D. Drijard, *et al*, Int. Conf. on High Energy Physics (Brighton, 1983).
30. D. Drijard, *et al*, Phys. Lett. B 81 (1979) 250.
31. D. Drijard, *et al*, Phys. Lett. B 85 (1979) 452.
32. P. Weilhammer, Int. Symposium on Multiparticle Dynamics (Tashkent, 1987).
33. M. Basile, *et al*, Nuovo Cimento A 63 (1981) 230.
34. M. Basile, *et al*, Nuovo Cimento A 65 (1981) 457.
35. M. Basile, *et al*, Nuovo Cimento A 67 (1981) 40.
36. P. Chauvat, *et al*, Phys. Lett. B 199 (1987) 304.
37. W. Lockman, *et al*, Phys. Lett. B 85 (1979) 443.
38. A. Clark, *et al*, Phys. Lett. B 77 (1978) 339.

39. A. Chilingarov, *et al*, Nucl. Phys. B 151 (1979) 29.
40. D. Antreasyan, *et al*, Phys. Rev. Lett. 45 (1980) 863.
41. H. Fischer, W. Geist, Z. Phys. C 19 (1983) 159.
42. J. Gunion, Phys. Lett. B 88 (1979) 150.
43. J. Collins, *et al*, Nucl. Phys. B 263 (1986) 37.
44. J. Cudell, *et al*, Phys. Lett. B 175 (1986) 227.
45. B. Combridge, Nucl. Phys. B 151 (1979) 429.
46. V. Barger, *et al*, Phys. Rev. D 25 (1982) 112.
47. R. Ordorico, Phys. Lett. B 107 (1981) 231.
48. J. Collins, *et al*, Nucl. Phys. B 263 (1986) 37.
49. R. Ellis, Preprint FERMILAB-CONF-86/35-T (1986).
50. S. Brodski, *et al*, Summer study on the Design and Utilisation of the SSC,
ed. R. Donaldson and J. Morfin.
51. R. Phillips, Proc. Second Moriond Workshop on New Flavours, Les Arcs,
France (Paris: Editions Frontiers) (1982) 463.
52. I. Peruzzi, *et al*, Phys. Rev. Lett. 37 (1976) 569.
53. G. Feldman, *et al*, Phys. Rev. Lett. 38 (1977) 1313.
54. G. Goldhaber, *et al*, Phys. Lett. B 69 (1977) 503.
55. M. Derrick, *et al*, Phys. Rev. Lett. 53 (1984) 1971.
56. M. Aguilar-Benitez, *et al*, Phys. Lett. B 169 (1986) 106.
57. R. Schindler, *et al*, Phys. Rev. D 24 (1981) 78.
58. M. Weber, "*D* Meson Production in 800 GeV/c PP Collisions", (Ph.D.
diss., University of Michigan, 1988)

59. J. Cudell, *et al*, Phys. Lett. B (1986) 227.
60. M. Weber, "*D* Meson Production in 800 GeV/c PP Collisions", (Ph.D. diss., University of Michigan, 1988) Calculations for Figures 22 and 23 produced by P. Bhat, Duke University